Determining the access to H-mode in the ITER pre-fusion and fusion power operation phases at low plasma current with full-radius TGLF-SAT2 simulations of L-mode plasmas

PAPER • OPEN ACCESS

Determining the access to H–mode in the ITER pre–fusion and fusion power operation phases at low plasma current with full–radius TGLF–SAT2 simulations of L–mode plasmas

To cite this article: C. Angioni *et al* 2023 *Nucl. Fusion* **63** 126035

OPEN ACCESS
IOP Publishing | International Atomic Energy Agency
Nuclear Fusion
Nucl. Fusion **63** (2023) 126035 (19pp)
https://doi.org/10.1088/1741-4326/acfdb9

Determining the access to H–mode in the ITER pre–fusion and fusion power operation phases at low plasma current with full–radius TGLF–SAT2 simulations of L–mode plasmas

C. Angioni[1,*], J. Citrin[2,3], A. Loarte[4], A.R. Polevoi[4], S.H. Kim[4], E. Fable[1] and G. Tardini[1]

[1] Max–Planck–Institut für Plasmaphysik, Boltzmannstrasse 2, D–85748 Garching, Germany
[2] DIFFER—Dutch Institute for Fundamental Energy Research, De Zaale 20, 5612 AJ Eindhoven, Netherlands
[3] Science and Technology of Nuclear Fusion Group, Eindhoven University of Technology, 5612 AZ Eindhoven, Netherlands
[4] ITER Organization, Route de Vinon-sur-Verdon, CS 90 046, 13067 St Paul Lez Durance, France

E-mail: clemente.angioni@ipp.mpg.de

Received 15 June 2023, revised 4 September 2023
Accepted for publication 27 September 2023
Published 17 October 2023

Abstract

The pre–fusion power operation 1 phase of ITER is planned to be characterized by electron cyclotron resonance heating only. Under the assumption that the access to H–mode is determined by a critical ion heat flux at the plasma edge, full–radius ASTRA simulations with the TGLF–SAT2 transport model are performed in order to compute the ion heat flux produced by the thermal exchange between electrons and ions in different operational conditions. Both hydrogen and deuterium plasmas at 5 MA are considered, respectively at 1.8 T and 2.65 T, corresponding to one third and half of the nominal maximum magnetic field. Different levels of electron cyclotron heating power are considered in sets of simulations with increasing values of the electron line averaged density. The predictions are compared with the currently available scaling of the critical ion heat flux. In hydrogen, 20 MW of electron heating power are predicted to allow H–mode access in a vanishingly small density window, whereas 30 MW and 40 MW would allow more substantial H–mode operational windows. Despite the fact that in deuterium plasmas the thermal exchange between electrons and ions is smaller by the hydrogen to deuterium mass ratio compared to hydrogen plasmas, the lower H–mode power threshold in deuterium leads to the prediction that an even broader and more robust domain to access H–mode is obtained at half field at 40 MW in deuterium as compared to operation in hydrogen at one third of the maximum magnetic field, even at the same power.

* Author to whom any correspondence should be addressed.

Keywords: ITER H-mode access low current, integrated transport modeling, electron heated tokamak plasmas

(Some figures may appear in colour only in the online journal)

1. Introduction

The ITER research plan foresees the investigation of H–mode access and sustainment in the initial phase of Pre–Fusion Power Operation 1 (PFPO–1) [1, 2]. During this initial phase, which is currently planned to be performed with hydrogen plasmas at 5 MA and 1.8 T, that is, at one third of the nominal maximum current and magnetic field of the ITER baseline scenario, it is foreseen that ITER will be equipped by Electron Cyclotron Resonance Heating (ECRH) only.

The minimum heating power which is required to access H–mode is usually observed to exhibit a non–monotonic dependence as a function of the plasma density [3–9], which is particularly evident in conditions of electron heating only. Such a non–monotonic dependence allows the identification of a density range with minimum power threshold, as well as of low and high density branches, which are characterized by heating powers to enter H–mode which respectively decrease and increase with increasing density. The non–monotonic dependence also implies a corresponding deviation in the low density branch from the multi–machine scaling law for the H–mode power threshold [10], which has been determined within the International Tokamak Physics Activities (ITPA) and has been specifically developed for the high density branch only.

Within the experimentally supported paradigm that the L–H transition is caused by turbulence stabilization produced by a sufficiently strong $E \times B$ rotational shear [11–13], the mechanisms which lead to the generation of the radial electric field become of critical importance. Several mechanisms can contribute to the development of a rotational shear at the plasma edge, leading to the required shearing rate to trigger the transition. These also include ion orbit losses [14, 15] and turbulence generated zonal flows [16]. Under the consideration that the leading role is played by the equilibrium radial electric field, which forms as a consequence of the evolution of the radial profiles of density, temperature, poloidal and toroidal rotations of the main ions, with increasing heating power the dominant contribution at the edge is played by the diamagnetic rotation term, provided by the main ion pressure gradient. In this term both the main ion logarithmic density gradient and the main ion temperature gradient appear, the latter directly connecting the strength of the radial electric field with the heating power that goes to the ions [17, 18]. This idea has received experimental confirmation at ASDEX Upgrade (AUG) [17, 19], through a study that has experimentally identified the critical role of the ion heat flux to access the H–mode. In the presence of auxiliary electron heating only, the ion heating power is exclusively provided by the thermal exchange from the electrons to the ions, which therefore is expected to play a critical role in determining the transition. The physical dependencies of the thermal exchange in combination with those of the energy confinement time in L–mode, as obtained in the scaling laws for global confinement times, allows the determination of the density at which the minimum power threshold occurs [17, 18], that, from now on, we simply refer to as the minimum density. Analysis of the C-Mod results have confirmed the critical role of the ion heat flux in determining the L–H transition [20], allowing the derivation of a scaling law for the critical ion heat flux at the L–H threshold, which combines AUG and C–Mod observations and that we shall call the Schmidtmayr scaling. Within this framework, the condition to exceed the heating power threshold to access H–mode becomes a condition to exceed a critical ion heat flux. In the presence of auxiliary electron heating only, the ion heat flux is exclusively determined by the density and temperature profiles, that is, it is completely determined by the transport properties of the plasma in combination with the heating and particle sources. Therefore, within the present approach, the determination of the H–mode existence domain becomes a transport problem, in which, from the predicted density and temperature profiles, the ion heat flux can be derived and can be compared to the Schmidtmayr scaling. With constant auxiliary electron heating, the increase of the plasma density progressively increases the ion heat flux, potentially crossing the Schmidtmayr scaling and therefore allowing the H–mode to be accessed. To this end, in [2], a simple transport model based on the L–mode confinement scaling law [21] was applied, with the additional condition of equal ion and electron heat conductivities. This approach allowed the calculation of the corresponding ion heat flux at the plasma edge, within these transport assumptions. Here that approach is repeated with simulations with the ASTRA transport code [22, 23] in which the turbulent transport is predicted by the TGLF–SAT2 [24, 25] transport model. The TGLF model [26, 27] has been recently upgraded to include the poloidal variation of the turbulence intensity in the saturation rule, practically leading to the solution of the previously observed limitation of reduced predicted transport in the peripheral region [24, 25]. The solution of the edge transport shortfall problem has allowed this model to be applied at AUG in a recent large set of validation studies [28, 29], also specifically dedicated to the modeling of experimental conditions which reproduced those expected in the ITER PFPO–1 phase [30]. The successful validation of this model for AUG L–mode plasma predictions over the entire minor radius, only using engineering parameters as input, in a wide variety of experimental conditions, particularly including those with ECRH only, and with respect to variations of all the main engineering parameters, gives confidence to the applicability of this model for a theory–based prediction of the density and temperature profiles of the ITER PFPO–1 hydrogen and Fusion Power Operation 1 (FPO–1) deuterium L–mode plasmas. From these predictions, the ion heat flux at the

plasma edge is computed and compared to the Schmidtmayr scaling to determine the conditions which allow H–mode operation.

The initial phases of ITER operation have already been subject of highly integrated modeling activities, in particular with the JINTRAC suite of codes for combined core and SOL/divertor modeling [31]. These studies have covered both the first phase with ECRH only at one third of the nominal magnetic field and the following phase at half of the nominal magnetic field with additional Neutral Beam Injection (NBI) heating [32, 33]. Very recently, integrated transport simulations have been also dedicated to ITER PFPO discharge scenarios in order to explore the operational space for long pulse operation [34].

The prediction of the power requirements to access H–mode in low density hydrogen plasmas with a metallic wall is complicated by three additional aspects with respect to the more usual situation of deuterium plasmas at high density in carbon walls, which is described by the multi-device ITPA scaling law [10]. The first aspect is that with metallic walls at AUG and JET–ILW the power threshold has been observed to be reduced with respect to previous operation with carbon walls and therefore also in comparison to the Martin's scaling, by 25% in AUG [7] and up to 40% in JET [8]. While some explanations for the observed reductions of power threshold have been proposed [35, 36], it can be considered that it is still unclear which physics will prevail in ITER and how the power threshold in ITER will behave in comparison to the extrapolations based on the ITPA scaling law. The second aspect is given by the fact that in several experiments a low density branch is observed in which the L–H power threshold increases with increasing density [3–9]. The increase of the power threshold below the density minimum can vary depending on conditions, up to situations in which no low density branch is observed. The third aspect is that the L–H power threshold in hydrogen is larger than that in deuterium by an amount which can vary depending on conditions, including the density range [7, 19, 37–43].

The following possible operational scenarios have been considered. For hydrogen plasmas, central ECRH of 20 MW, as currently foreseen, as well as 30 MW and 40 MW, at one third of the magnetic field and of the plasma current of the ITER baseline full field scenario, that is at 5 MA and 1.8 T, with the ITER baseline safety factor $q_{95} = 3$. For deuterium plasmas, a total ECRH of 40 MW, deposited half in the center and half at mid–radius, has been considered, at 5 MA and 2.65 T, corresponding to $q_{95} = 4.4$, as a representative initial deuterium plasma in FPO–1. In section 2 the simulation set–up is described. The results at 20 MW of ECRH power for a hydrogen plasma are presented in section 3, together with the analysis of the impacts of different assumptions, such as those regarding the boundary conditions for the electron density and the ion temperature, as well as of the inclusion of an additional impurity. In section 4 the corresponding results for density scans in hydrogen plasmas with increasing levels of ECRH power are shown. Here also the impact of the removal of the $E \times B$ shearing rate is discussed. Section 5 shows the corresponding results for the deuterium plasmas with 40 MW of ECRH at 2.65 T and 5 MA. Finally, in section 6 the main results of all the considered scenarios are compared. This will allow us to draw some conclusions on the possibility of accessing H–mode in the ITER PFPO–1 and FPO–1 phases in the various conditions which have been examined, of course within the framework of the assumptions of this study.

2. Modeling set–up

The transport code ASTRA [22, 23] is used with the transport model TGLF–SAT2 [24, 25]. The modeling approach follows the set–up described in [28, 29]. In the case of these ITER L–mode simulations, a radial grid of 161 equidistant points is used in ASTRA, with correspondingly 80 equidistant radial calls of TGLF–SAT2, at each second ASTRA radial grid point. An interpolation and a light smoothing is then applied to pass from the radial grid of TGLF–SAT2 calls to the ASTRA radial grid. Boundary conditions are set at the separatrix. Scalings for the electron and ion temperature at the separatrix based on a set of SOLPS simulations have been reported in [44], showing that these depend on the scrape–off layer and divertor parameters, with a specific dependence on the power crossing the separatrix. Following equations 7 and 8 in [44], and considering a variation of the power through the separatrix from 20 MW to 40 MW, as well as a variation of the electron to ion heat flux ratio, the separatrix electron and ion temperatures at the separatrix can approximately vary from 90 eV to 125 eV and from 110 eV to 180 eV respectively. Consistently with [2], a separatrix electron temperature of 120 eV is assumed. The ion temperature is assumed to be the same as the electron temperature, additional simulations are performed to test the impact of an increase of the separatrix ion temperature. To gauge the effect, a high ion temperature of 200 eV has been considered. We underline that this value is not considered here to be an upper limit for the ion to electron temperature ratio at the separtrix in these ITER plasmas, but just a, likely large, value which has been chosen to gauge the effect of a change in this parameter. Since also the applicability of the scalings derived in [44] to the ITER PFPO conditions is unclear, two sets of additional simulations have been performed, one with separatrix electron and ion temperatures of 90 eV, and one with electron and ion separatrix temperatures at 90 eV and 150 eV respectively. The comparison of these simulations have shown that the density windows which allow access to H–mode as well as the excess of ion heat flux in comparison to the scaling for the L–H transition are weakly dependent on the actual value of the separatrix electron temperature, 90 eV or 120 eV, but are strongly affected by an increase of the ion temperature, which reduces the ion heat flux. For this reason, in the following, only results with electron temperature at the separatrix of 120 eV are shown, but, at the same time, results with a ion temperature at the separatrix of both 120 eV and 200 eV are presented.

Density scans are performed, in which the separatrix density is progressively increased, keeping approximately constant the ratio between the line averaged density and the separatrix density. The simulations are performed in order to produce

different levels of the line averaged density by matching the requested density with a feed–back on the gas puff rate at the edge [28]. A set of nine levels of plasma densities are usually considered, from 0.6 10^{19} m^{-3} up to around 4.0 10^{19} m^{-3}. We recall that the Greenwald density limit [45] at 5 MA corresponds to 4.0 10^{19} m^{-3}. The impact of an increase of the separatrix density is also specifically investigated, by changing the assumed ratio between the requested line averaged density and the separatrix density. The gas puff rate, which is required to provide a given line averaged density, decreases with increasing assumed separatrix density. It is important to add that, within this work, which is exclusively dedicated to the transport behavior of the confined plasma, the compatibility of any assumed separatrix density with the requirements for power exhaust has not been considered.

The heating powers on the electrons include the auxiliary electron heating power from ECRH and the consistently computed Ohmic power and the radiation losses. The ions are exclusively heated by the thermal exchange from electrons to ions. Given the uncertainties in the amount of neutral particles present in the edge region, which in the simulation are determined by the requirements of matching the desired line averaged density, energy sources and losses coming from ionization and charge–exchange have been neglected. These are not completely negligible at low density for the ions close to the separatrix, and reduce the ion heat flux in the most external region up to about 1 MW at the separatrix, but already have a much smaller impact on the ion heat flux at $\rho_{tor} = 0.95$, position at which the experimental ion heat fluxes have been evaluated for the Schmidtmayr scaling. Neutral energy sources and losses only have a very small impact on the ion temperature predictions. Given the overall uncertainties, including those regarding the relevant radial position for the evaluation of the ion heat flux in comparison with the Schmidtmayr scaling, the approach of neglecting ionization sources and charge–exchange losses is considered appropriate.

Beryllium impurity is included in the modeling, with fixed in time and constant in radius concentration equal to 4.2%, providing a $\Delta Z_{\rm eff} = 0.5$. The radiated power is computed as provided by the Bremsstrahlung radiation consistent with a $Z_{\rm eff} = 1.5$. While the beryllium density profile is not evolved in the simulation, its effect on the TGLF–SAT2 ion and electron turbulent fluxes is taken into account, by including the beryllium impurity as an additional species in the TGLF-SAT2 input. The impact of the inclusion of an additional radiating impurity is considered in section 3. An example of the electron and ion heat fluxes, where also the neutral density ionization and charge–exchange ion energy sources are included, is presented in figure 1, for a plasma with 30 MW of ECRH at line averaged density of 1.9 10^{19} m^{-3}.

For simplicity the ECRH beams are considered to produce negligible current drive, and no electron cyclotron driven current is included in the poloidal magnetic field equation. This would in any case modify only the inner part of the safety factor profile, where only a very small amount of power is thermally exchanged from electrons to ions. The current density profile is evolved in time and a sawtooth period model is included, which flattens the current density and the safety factor profiles inside the sawtooth inversion radius every 100 ms.

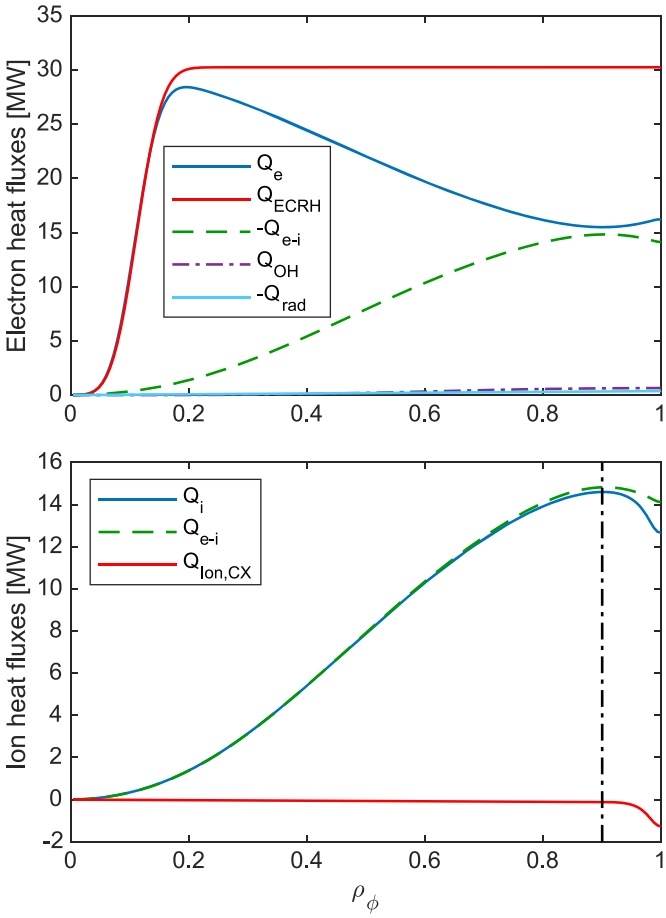

Figure 1. Radial profiles of the electron (*a*) and ion (*b*) heat flux contributions with 30 MW central ECRH from a ASTRA/TGLF–SAT2 simulation of a ITER hydrogen plasma at 5 MA and 1.8 T and 1.9 10^{19} m^{-3} line averaged density, as a function of the normalized toroidal minor radius ρ_ϕ. To assess the size of ion energy losses from charge exchange and sources from ionization, these have been included in the curves in plot (*b*), but are neglected in the simulations of the rest of this paper.

The equipartition power is consistently computed within ASTRA with the following formula for a multi–species plasma

$$P_{e-i} = 0.00246 \log\Lambda \frac{T_e - T_i}{T_e^{3/2}} n_e \sum_j n_j \frac{Z_j^2}{A_j}, \qquad (1)$$

with power in MW, temperatures in keV and densities in 10^{19} m^{-3}, and where $\log\Lambda = 15.9 - 0.5\log n_e + \log T_e$ is the Coulomb logarithm. The sum on j is applied to all the ion species, which are assumed to have the same temperature T_i.

As it can be expected, while an increase of the separatrix ion temperature decreases the ion heat flux produced by the electron to ion thermal coupling at the edge, an increase of the separatrix density has the opposite effect of increasing the coupling in the peripheral region and therefore increasing the ion heat flux. However, for a given line averaged density, there is a maximum separatrix density which allows

that line averaged density to be obtained, and which corresponds to zero gas puff rate. As it has been demonstrated in [28], TGLF–SAT2 predicts the existence of an inward convection at the plasma boundary, which leads to the prediction of a finite particle content with zero particle source inside the plasma and finite separatrix density. Clearly the separatrix density that provides a given line averaged density with zero particle source is the highest separatrix density possible for that same line averaged density, according to TGLF–SAT2. This can be understood from the fact that the plasma particle outflux is zero, since there is no particle source in the plasma, and therefore this situation corresponds to the flattest density profile from the separatrix inward. This property provides an additional degree of freedom in computing the ion heat flux at the boundary, considering that it is presently difficult to precisely predict which separatrix density ITER will have in this type of plasmas. This aspect of the problem has been specifically considered below in section 3, determining the existence domain of the values of separatrix density which are admitted by TGLF–SAT2 for each value of line averaged density.

The radial electric field, and the consequent $E \times B$ shearing rate effect on the TGLF–SAT2 results, is consistently included in this set of simulations, and it is provided by the sum of the diamagnetic and the neoclassical poloidal rotation terms. The poloidal rotation is computed with NCLASS [46], the toroidal rotation is assumed to be equal to zero. The impact of the neglect of the $E \times B$ shearing rate will be specifically discussed in section 4.

3. Density scans with 20 MW ECRH hydrogen plasma

In figure 2 we present an example of the results for a scan over nine values of the line averaged density, from 0.66 10^{19} m^{-3} to 3.46 10^{19} m^{-3}, with a low separatrix density $n_{e,\mathrm{sep}}$, assumed to be about 5.5 times smaller than the requested line averaged density $n_{e,\mathrm{lin}}$. and an auxiliary heating power of 20 MW of ECRH deposited close to the magnetic axis, at $\rho_\phi = 0.1$. Simulations are run for 8 s of the ASTRA simulation time, with a time step of 25 ms, and a call of TGLF–SAT2 every second ASTRA time step. The final results are taken averaging over the last two seconds of the simulation, where stationary conditions are reached, with the particle and heat fluxes which match the corresponding volume integrals of the sources. The relatively long time step still remains significantly shorter than the predicted confinement times of these simulated ITER plasmas, which increase from about 160–200 ms at the lowest densities to about 900 ms at the highest densities. The increase of the confinement time with increasing density reveals that these ITER plasmas are predicted to largely belong to the linear confinement regime with respect to a density increase, at least in the low density range, up to approximately 2.5 10^{19} m^{-3}. Moreover, it is important to recall that ASTRA applies a fully implicit numerical scheme, which has been specifically developed for stiff transport models [47] and which allows large time steps to be used in order to quickly and robustly reach convergence to stationary flux–matching conditions.

The results of figure 2 can be considered to provide a first example of full–radius ASTRA/TGLF–SAT2 results of ITER PFPO–1 plasmas, in complete analogy to figure 2 of [2], which, instead of TGLF–SAT2, adopted the conditions of $\chi_i = \chi_e$ and of matching the IPB98 scaling law for L–mode confinement [21]. The analysis of the profiles of the electron and ion heat fluxes, shown in figures 2(*d*) and (*e*) respectively, is of interest. We observe that, despite the assumption of equal ion and electron temperatures of 120 eV at the separatrix, with increasing density the ion temperature starts to exceed the electron temperature at the periphery, with consequent reduction of the ion heat flux in the peripheral region, as visible in figure 2(*e*). This behavior can be considered to be practically unavoidable for sufficiently close ion and electron heat conductivities. One can observe that around $\rho_\phi = 0.8$, at sufficiently high density, the ion heat flux starts to exceed the electron heat flux, while the number of ion particles is lower than the number of electrons, with a $Z_{\mathrm{eff}} > 1$. Therefore, at sufficiently high density, outside a certain minor radius at the plasma periphery, the ion heat flux per particle becomes larger than the electron one, leading to ion temperatures which start to exceed the electron temperatures. This reverses the direction of the thermal positive heat flux exchange, from electrons to ions to from ions to electrons. Of course, while the computation of the heat fluxes within these simulations can be considered to be exact, there is a large uncertainty in the determination of the heat exchange at the periphery from an experimental standpoint. The results from [17] and [20] consider the ion heat flux at $\rho_\phi = 0.95$, this is why in (e) both the flux at the separatrix $\rho_\phi = 1$ and at $\rho_\phi = 0.9$, which envelop the value of the experimental analysis, have been plotted. For low values of the line averaged density, the difference between the ion heat fluxes at $\rho_\phi = 0.9$ and $\rho_\phi = 1.0$ is practically negligible, and therefore the precise radial position at which the ion heat flux is considered becomes irrelevant.

The values of the ion heat fluxes are compared with the Schmidtmayr scaling [20], which was obtained for deuterium plasmas. How one can exactly translate the Schmidtmayr scaling to hydrogen plasmas is not obvious. On AUG, in power balance analyses at the L–H transition of a set of low density ECRH plasmas, the difference in ion heat flux between corresponding deuterium and hydrogen plasmas has been found to be a factor 2.5 [19]. A factor larger than 2 between the hydrogen and the deuterium ion heat fluxes at the transition has been confirmed in more recent experiments in AUG [37, 38], with ratios even approaching 3 in the electron density range around the density minimum, without significant differences between ECRH and NBI heating. These observations are less favorable for H–mode access in hydrogen with respect to the difference between the power thresholds in the high density branch. This is usually reported to be about a factor of 2 larger in hydrogen than in deuterium [7, 39] although results have been obtained in which this ratio can significantly exceed 2 [38, 40–43]. Recently, an analogous power balance analysis at the L–H transition in a low density DIII-D plasma, in this case with NBI heating, has reported a ratio between H and D around

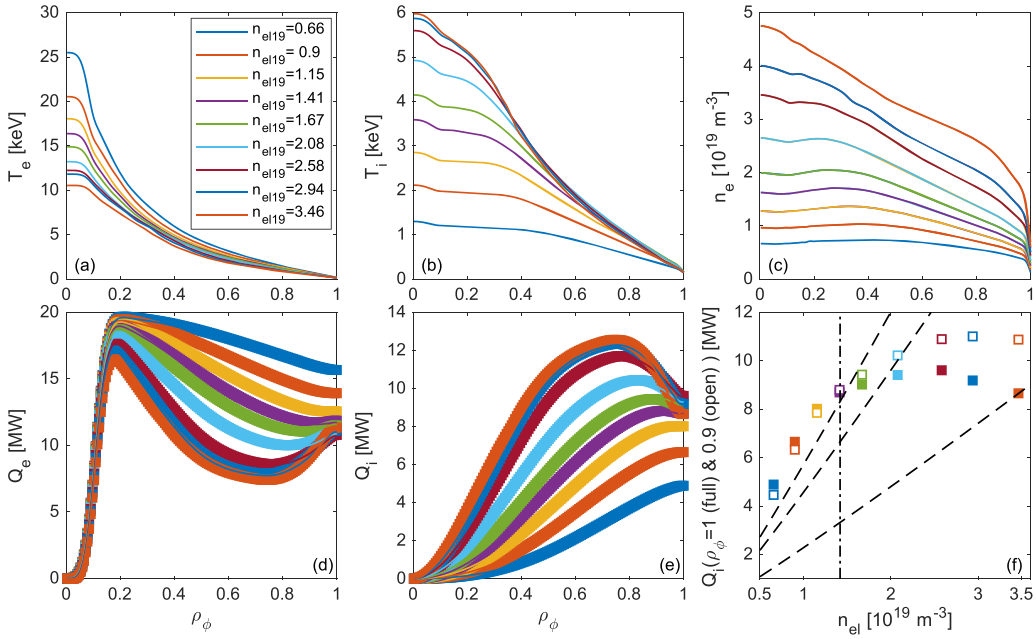

Figure 2. ASTRA/TGLF–SAT2 predictions of the electron temperature (*a*), the ion temperature (*b*) in keV, and the electron density (*c*) in 10^{19} m^{-3} in ITER hydrogen plasmas at 5 MA and 1.8 T, with 20 MW of ECRH power as a function of the normalized toroidal minor radius ρ_ϕ, for different prescribed values of the line averaged electron density, reported in the legend. The corresponding profiles of the electron and ion heat fluxes are presented in (*d*) and (*e*). In (*f*) the corresponding values of the ion heat fluxes at $\rho_\phi = 1$ and $\rho_\phi = 0.9$ are plotted as a function of the line averaged density. In (*f*) the oblique dashed line correspond to 1.0, 2.0 and 2.5 times the Schmidtmayr scaling for the ion heat flux for the L–H transition in a deuterium plasma, while the vertical dash–dotted line identifies the line averaged density value where the minimum density is expected to occur according to [17].

2 in the ion heat fluxes at the L–H transition [43]. We consider therefore that, although the ratio 2.5 has been obtained in present experiments with the same type of heating foreseen in the ITER PFPO–1 phase, and therefore in the absence of NBI driven plasma rotation, also a ratio 2 can be, more favorably, considered in the present analysis. For the hydrogen L–H power threshold, following the usual approach, we consider a factor 2 with respect to the Martin's scaling for deuterium plasmas, keeping in mind that there are observations in which this factor can even exceed 3. An additional element, that it is important to consider, is that in metal wall devices like AUG and JET, the power threshold has been observed to be reduced by approximately 25% in AUG [7] and up to 40% in JET [8] with respect to the previous corresponding levels in graphite walls, which are described by the Martin's scaling law.

3.1. Variation of the separatrix density in 20 MW ECRH hydrogen plasma

We explore then the impact of increasing $n_{e,\mathrm{sep}}$ at the same $n_{e,\mathrm{lin}}$, by producing additional density scans, one with a ratio of $n_{e,\mathrm{lin}}$ to $n_{e,\mathrm{sep}}$ equal to 3.5, and one in which $n_{e,\mathrm{sep}}$ is increased with zero gas puff, that is, zero particle source in the confined plasma. Such a $n_{e,\mathrm{sep}}$ scan with zero particle source allows us to identify the TGLF–SAT2 predicted minimum line averaged density which can be obtained with a given separatrix density, or, reciprocally, the maximum separatrix density which is compatible with a given line averaged density. The domain of possible separatrix densities for each given line averaged density is presented in figure 3(*a*), where also the results with two different ratios of line averaged to separatrix density are reported. This plot could be completed with a lower boundary for the separatrix density which is provided by the requirement of power exhaust into the divertor and which depends on the power outflux in combination with other edge parameters [44]. As it has been already mentioned, the determination of this lower limit is out of the scope of the present work.

The corresponding values of ion heat fluxes, always with an auxiliary heating of 20 MW of ECRH power, for these three different separatrix densities and gas puff conditions, are plotted in figure 3(*b*). As expected, the ion heat flux at the edge increases with increasing edge density, since in the peripheral region the thermal exchange between electrons and ions becomes stronger. We observe however that a separatrix density which is approximately one third of the line averaged density already provides ion heat fluxes levels which are close to those which can be obtained in the upper limit provided by the maximum allowed separatrix density, corresponding to zero particle flux.

In figure 3(*a*) it is interesting to note that a clear change of slope is obtained in the relation between separatrix density and line averaged density with zero particle source. This corresponds to a change of the density profile shape in the presence of electron heating, which is hollow over a large portion of the minor radius at low density and high electron heating power per particle, whereas it becomes peaked at high density, with reduced electron heating power per particle and increased ion heat flux in the plasma. This modification of the density profile

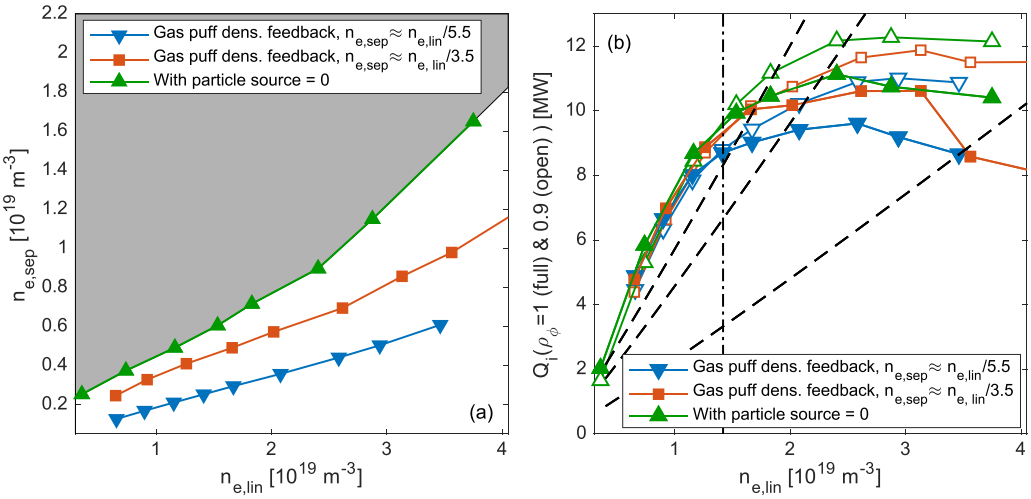

Figure 3. In (*a*), ASTRA/TGLF–SAT2 predictions of the range of values of the separatrix density, on the *y*–axis, which are possible for each given value of the line averaged density, on the *x*–axis. Above a certain value of the separatrix density, which is predicted to provide the line averaged density with zero particle source in the confined plasma, it is not possible to obtain a requested value of the line averaged density, due to the TGLF–SAT2 prediction of an inward convection at the separatrix. The inaccessible region is covered in gray in (*a*). In (*b*), the ion heat fluxes in MW at $\rho_\phi = 1$ and $\rho_\phi = 0.9$, respectively in full and open symbols, corresponding to the ratio of the line averaged density to separatrix density equal to 5.5 (triangles pointing down), equal to 3.5 (squares) and without any gas puff (zero particle source in the confined plasma, triangles pointing up) are shown with the same symbols as in (*a*), as reported in the legends. In (*b*) the vertical dash–dotted line corresponds to the minimum density according to [17], whereas the three oblique dashed lines correspond to 1, 2 and 2.5 times the ion heat flux scaling of [20] for the L–H transition.

shape reflects a transition in the dominant turbulence along the minor radius from trapped electron mode to ion temperature gradient mode with increasing density [48, 49], which is also observed experimentally [50].

The impact of an increased ion temperature at the separatrix is assessed through an additional scan with $T_{i,\mathrm{sep}} = 200\,\mathrm{eV}$, while keeping $T_{e.\mathrm{sep}} = 120\,\mathrm{eV}$, again with $n_{e,\mathrm{sep}} = n_{e,\mathrm{lin}}/5.5$. By combining such a large separatrix ion temperature with a low separatrix density, we consider that this case provides the most unfavorable condition to obtain a large ion heat flux.

The summary of the results at 20 MW of ECRH, moving from such an unfavorable condition to the most favorable condition to maximize the ion heat flux at the edge, with $T_{e.\mathrm{sep}} = T_{i,\mathrm{sep}} = 120\,\mathrm{eV}$ and large separatrix density is presented in figure 4, where the difference between ion heat fluxes at $\rho_\phi = 1.0$ and $\rho_\phi = 0.9$ and the corresponding L–H ion heat flux threshold times 2.5 and 2.0 from the Schmidtmayr scaling are plotted in (*a*) and (*b*) respectively.

As it can be observed, in these conditions, in which the density window where the ion heat flux exceeds the Schmidtmayr scaling is at low density, there is no large difference in the results obtained considering the ion heat flux at $\rho_\phi = 1.0$ and those obtained considering the ion heat flux at $\rho_\phi = 0.9$. This reduces the uncertainties at least from the standpoint of the radial location of the ion heat flux which is the most relevant to lead to the L–H transition. If a hydrogen threshold equivalent to 2.5 times the Schmidtmayr ion heat flux scaling for deuterium is considered, figure 4(*a*), the predicted density window is strongly limited below 1.7 $10^{19}\,\mathrm{m}^{-3}$, consistent with the density at which twice the Martin's scaling law for the high density branch of the L–H transition in deuterium reaches 20 MW, equal to 1.63 $10^{19}\,\mathrm{m}^{-3}$. In contrast, with an ion heat flux threshold in hydrogen equal to only 2.0 times the Schmidtmayr ion heat flux scaling for deuterium, the density window reaches 2.3 $10^{19}\,\mathrm{m}^{-3}$, providing a slightly broader range of operation. Within these comparisons on the density window, the already mentioned reduction of the power threshold, which has been observed in AUG and JET with metal walls as compared to the previous power requirements with graphite walls, is also of interest. With a reduction of 25% of the power threshold, the density at which 1.5 times the Martin scaling is equal to 20 MW is 2.43 $10^{19}\,\mathrm{m}^{-3}$, more consistent with a factor 2 only increase of the deuterium ion heat flux condition. The minimum density for the L–H transition in deuterium according to [17] is at 1.42 $10^{19}\,\mathrm{m}^{-3}$, identified by a vertical dash–dotted line in figure 4. In terms of excess of the threshold ion heat flux, in the case of 2.5 times the deuterium Schmidtmayr scaling one can rely on less than 2 MW only, whereas in the case of 2.0 times the deuterium Schmidtmayr scaling the power range marginally reaches 3 MW. At these low densities, corresponding to the range between 0.25 and 0.50 the ITER Greenwald density at 5 MA, an L–H transition can be expected to directly produce a density increase. Therefore, it can also be expected that, even in the event of a limited increase in density, in such a restricted H–mode operational window in density and power, this is likely to lead to an H–L back–transition. The present analysis for a 5 MA hydrogen plasma, which uses full–radius ASTRA/TGLF–SAT2 predictions of the ion heat flux in comparison with 2 to 2.5 times the Schmidtmayr ion heat flux scaling for deuterium, leads to the conclusion that with 20 MW ECRH only an almost vanishing H–mode operational window can be expected, with practically no possibility of stable H–mode operation.

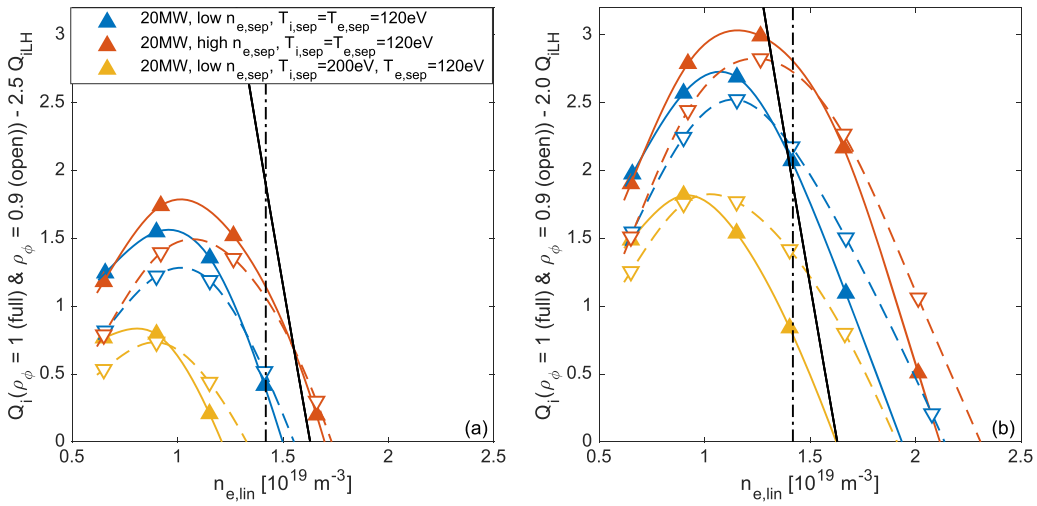

Figure 4. Ion heat fluxes in MW at $\rho_\phi = 1.0$ (full triangles pointing up) and at $\rho_\phi = 0.9$ (open triangles pointing down) minus the L–H transition Schmidtmayr ion heat flux scaling times 2.5 (*a*) and times 2.0 (*b*) as a function of the line averaged density, for hydrogen plasmas with 20 MW ECRH, as well as with $n_{e,\mathrm{sep}} \simeq n_{e,\mathrm{lin}}/5.5$ and $T_{i,\mathrm{sep}} = T_{e,\mathrm{sep}} = 120$ eV, with $n_{e,\mathrm{sep}} \simeq n_{e,\mathrm{lin}}/3.5$ and $T_{i,\mathrm{sep}} = T_{e,\mathrm{sep}} = 120$ eV, and with $n_{e,\mathrm{sep}} \simeq n_{e,\mathrm{lin}}/5.5$ and $T_{i,\mathrm{sep}} = 200$ eV and $T_{e,\mathrm{sep}} = 120$ eV, as reported in the legend. The vertical dash–dotted line identifies the minimum density according to [17], while the solid oblique line provides $20 - 2P_{\mathrm{LH,Martin}}$, again in MW.

3.2. Inclusion of additional radiating impurity in 20 MW ECRH hydrogen plasma

An additional set of simulations with only four density levels has been performed in order to investigate the impact of the inclusion of an additional radiating impurity. To this end, in addition to 4.2% concentration of beryllium, providing a $\Delta Z_{\mathrm{eff}} = 0.5$, a 2% concentration of Neon has been added in both the ASTRA plasma composition, with a consequent increase of Z_{eff} from 1.5 to 3.3, as well as in the species considered by TGLF–SAT2, which is now run with four fluid species. The calculations have been performed with $T_{i,\mathrm{sep}} = T_{e,\mathrm{sep}} = 120$ eV and a separatrix density given by $n_{e\mathrm{sep}} = n_{e\mathrm{lin}}/5$. The results are presented in figure 5 and can be compared to the corresponding ones in figure 2. We observe that the inclusion of an additional impurity leads to two concomitant effects which both cause a reduction of the ion heat flux at the edge. From the standpoint of the thermal exchange between electrons and ions, a simple manipulation of equation (1) which includes the quasi–neutrality condition, leads to the following expression

$$P_{e-i} = 0.00246 \log\Lambda \frac{T_e - T_i}{T_e^{3/2}} \times n_e^2 \frac{Z_i}{A_i} \left[1 + \sum_{z \neq i} \frac{n_z}{n_e} Z_z \left(\frac{Z_z}{A_Z} \frac{A_i}{Z_i} - 1 \right) \right], \qquad (2)$$

where the index i refers to the main ions only, while the index z to the impurity species, and the sum on $z \neq i$ is intended to be performed on all the impurity species only, without including the main ion species. In the right hand side of equation (2) one can identify the expression outside the squared brackets, which provides the equipartition power of the plasma without impurities, and the expression in the squared brackets which provides the factor produced by the presence of additional impurities. We observe that whether this factor is larger or smaller than one critically depends on the differences in the charge to mass ratio Z/A of the various ion species. If the impurities have the same Z/A as the main ions, what is typical for fully stripped light impurities in a deuterium plasma, the second term in the squared brackets is equal to zero, which leads to the result that the inclusion of impurities does not change the equipartition power with respect to a clean deuterium plasma. We notice that the same situation would occur in a He plasma, where also the Z/A of the main ion is equal to 1/2. In complete contrast, the situation is different with non–deuterium hydrogen isotopes. With hydrogen, $Z/A = 1$, the inclusion of impurities with $Z/A < 1$ reduces the strength of the coupling, which in hydrogen is at least two times stronger, leading to a reduction of the thermal exchange power between electrons and ions with respect to a clean hydrogen plasma. Opposite situation would be obtained in a tritium plasma, since the charge to mass ratio of the main ions $Z/A = 1/3$ is smaller than the usual ratio of fully stripped light impurities $Z/A = 1/2$, allowing the second term of the squared brackets in equation (2) to provide a contribution larger than one. In conclusion, the addition of impurities in a hydrogen plasma reduces the equipartition power. However this not the only effect. The presence of additional impurities also reduces the ion heat transport by dilution of the ion thermal drive, effectively producing lower heat conductivities, but also reduces the total number of ion particles, both effects leading to an increase of the ion temperatures. The synergistic combination of all of these effects causes a very strong reduction of the ion heat flux at the edge, as it can be observed in the ASTRA results presented in figure 5. These results can be directly compared with those of figure 2. At corresponding densities, with the same color code in the two figures, despite the increased radiated power, both electron and ion temperatures

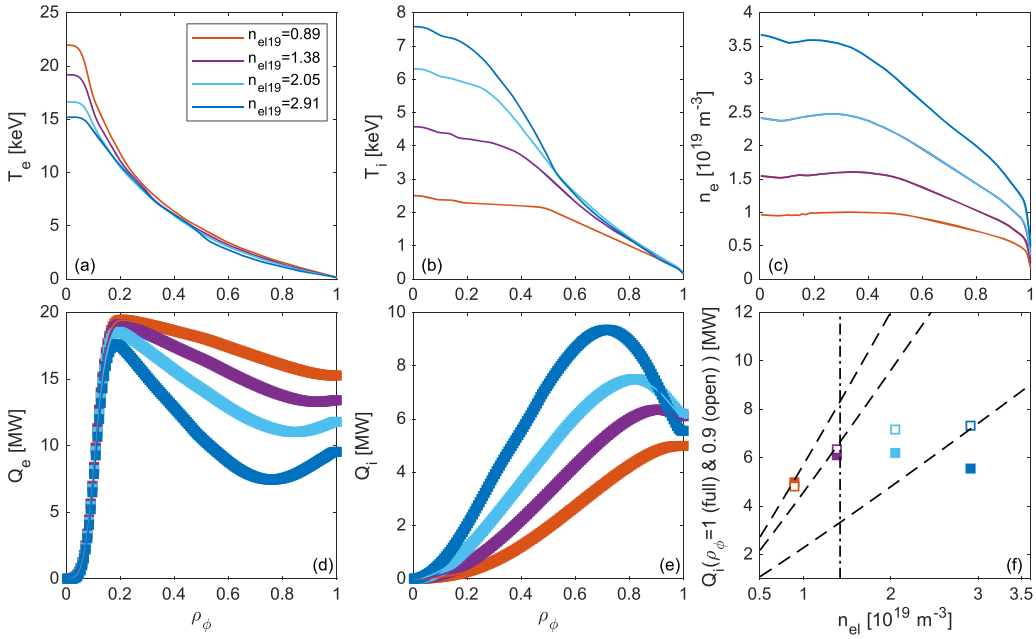

Figure 5. ASTRA/TGLF–SAT2 predictions of the electron temperature (*a*), the ion temperature (*b*) in keV, and the electron density (*c*) in 10^{19} m^{-3} in ITER hydrogen plasmas at 5 MA and 1.8 T, with the addition of 2% of neon and with 20 MW of ECRH power as a function of the normalized toroidal minor radius ρ_ϕ, for different values of the line averaged electron density, reported in the legend. The corresponding profiles of the electron and ion heat fluxes are presented in (*d*) and (*e*). In (*f*) the corresponding values of the ion heat fluxes at $\rho_\phi = 1$ and $\rho_\phi = 0.9$ are plotted as a function of the line averaged density. In (*f*) the oblique dashed line correspond to 1.0, 2.0 and 2.5 times the Schmidtmayr scaling for the ion heat flux for the L–H transition, while the vertical dash–dotted line identifies the line averaged density value where the minimum density is expected to occur according to [17].

are increased, as the concomitant consequence of the reduced heat transport and the decreased thermal transfer from electrons to ions. The overall consequence is a strong reduction of the ion heat flux at the edge, shown in figure 5(*f*), which remains even below the Schmidtmayr scaling times 2.5, and, only at very low density, marginally exceeds the Schmidtmayr scaling times 2.0. From this it can be concluded that in a hydrogen plasma, within the present modeling framework, the addition of impurities reduces the possibilities of exceeding the ion heat flux threshold to enter H–mode.

With 20 MW of auxiliary ECRH power additional simulations have been performed to assess the impact of replacing the hydrogen mass with the deuterium mass in the TGLF–SAT2 input. A negligible difference has been obtained in the low density cases, with the consequence that no significant difference is obtained in the predictions when the ion heat flux is compared to 2.5 times the Schmidtmayr scaling. With increasing density, the predicted reduction of density peaking in the core of deuterium plasma as compared to hydrogen plasmas, consistent with theoretical expectations in ion temperature gradient turbulence [51], has required an about three times increase of gas puff rate in deuterium to obtain the same line averaged density, with a consequent increase of the density in the periphery and a small increase of the ion heat flux. This provides a slight broadening of the density window, from 2.0 10^{19} m^{-3} to 2.5 10^{19} m^{-3}, which allows the ion heat flux to be above a factor 2 times the Schmidtmayr scaling (we remind here that for deuterium this factor is 1).

A last set of simulations has been performed to test different assumptions in the relaxation of the current density profile, also removing the sawtooth mixing model for the current density and safety factor profiles. Considering that this only impacts the central region of the plasma, where the thermal exchange power is small, no significant differences have been found in the predicted ion heat fluxes at the edge.

4. Results with increased ECRH power in 5 MA hydrogen plasmas

A companion set of simulations has been performed increasing the central ECRH power to 30 MW, again for a hydrogen plasma at 5 MA and 1.8 T. The results are presented in figure 6 and can be directly compared with the corresponding results at 20 MW presented in figure 4.

With 30 MW of ECRH power the access to H–mode is predicted to become possible over a relatively large density window, where, at sufficiently high density, the more favorable assumption of $T_{esep} = T_{isep}$ can be also considered to become more realistic. Depending on whether the Schmidtmayr scaling for deuterium is applied with a factor 2.5, figure 6(*b*), or with a factor 2.0, figure 6(*c*), the density window reaches 2.5 10^{19} m^{-3} and 3.0 10^{19} m^{-3} respectively, corresponding to 0.62 and 0.75 the Greenwald limit. The maximum excess of ion heat flux is now more directly centered around the density minimum value of the Ryter scaling (vertical dash–dotted

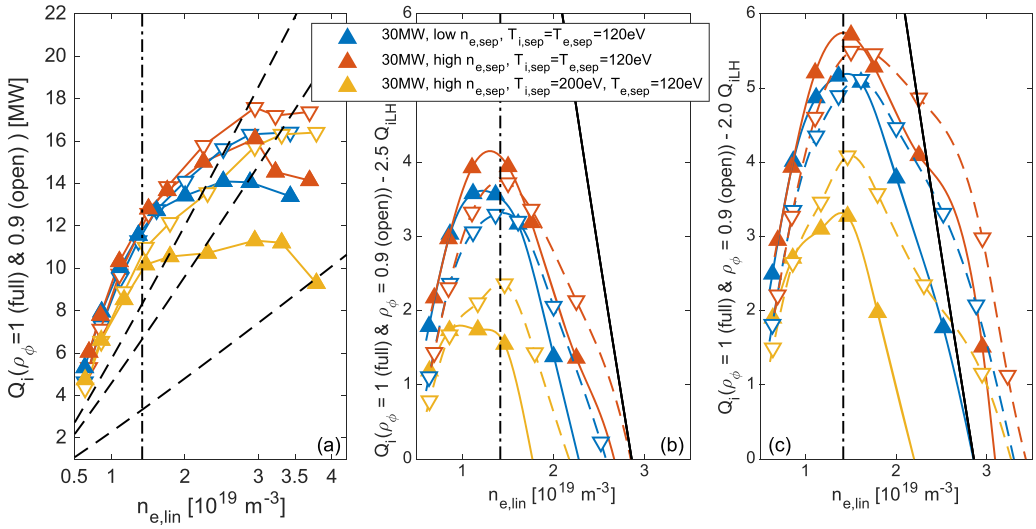

Figure 6. Ion heat fluxes in MW at $\rho_\phi = 1.0$ (full triangles pointing up) and at $\rho_\phi = 0.9$ (open triangles pointing down) (*a*), the same fluxes minus the L–H transition Schmidtmayr ion heat flux scaling times 2.5 (*b*) and times 2.0 (*c*) as a function of the line averaged density, for hydrogen plasmas with 30 MW ECRH, as well as with $n_{e,\mathrm{sep}} \simeq n_{e,\mathrm{lin}}/4.5$ and $T_{i,\mathrm{sep}} = T_{e,\mathrm{sep}} = 120$ eV, with $n_{e,\mathrm{sep}} \simeq n_{e,\mathrm{lin}}/2.8$ and $T_{i,\mathrm{sep}} = T_{e,\mathrm{sep}} = 120$ eV, and with $n_{e,\mathrm{sep}} \simeq n_{e,\mathrm{lin}}/2.9$ and $T_{i,\mathrm{sep}} = 200$ eV and $T_{e,\mathrm{sep}} = 120$ eV, as reported in the legend. The vertical dash–dotted line identifies the minimum density according to [17], while the solid oblique line provides $30 - 2P_{LH,\mathrm{Martin}}$, again in MW.

lines in 6) and reaches 3.5 MW and 5 MW with factors 2.5 and 2.0 to the Schmidtmayr scaling respectively. A situation with $T_{i\mathrm{sep}} > T_{e\mathrm{sep}}$ is still predicted to produce a strong reduction of the operational window in which the ion heat flux exceeds the scalings. With $T_{i\mathrm{sep}} = T_{e\mathrm{sep}}$, the density range at which the predicted ion heat flux is equal to 2 or 2.5 the Schmidtmayr scaling turns out to envelope the density value of 2.86 10^{19} m^{-3} at which two times the Martin scaling for P_{LH} is equal to 30 MW. In contrast, 1.5 times the Martin scaling for P_{LH} is equal to 30 MW at 4.3 10^{19} m^{-3}, therefore above the Greenwald limit, offering the prediction of a significantly broader operational window in density. In terms of powers, we observe that, with equal separatrix temperatures, the ASTRA/TGLF–SAT2 predicted ion heat flux exceeds 2.5 and 2 times the Schmidtmayr scaling for the ion heat flux up to 4 MW and 5.5 MW respectively, corresponding to a density which is close to the density minimum of the Ryter scaling. All of these considerations lead to the prediction that with 30 MW ECRH there is a finite operational window in density and power which allows H–mode to be accessed and maintained.

A final set of simulations has been performed with the hypothetically high ECRH power of 40 MW, again with central deposition, for a direct comparison with the other cases at lower ECRH powers. The comparison with the corresponding cases at 20 MW and 30 MW is presented in figure 7. This comparison shows that the maximum achievable ion heat flux does not scale linearly with increasing electron heating power, due to the fact that, for the same difference between electron and ion temperature, the equipartition power between electrons and ions decreases with increasing electron temperature, making the thermal exchange less efficient at higher electron temperature, and therefore at higher electron heating power. The sudden reduction of the predicted ion heat flux at the separatrix obtained with the last high density values in the scans reflects the start of the development of a pedestal in the temperature profiles of the TGLF–SAT2 predictions, with consequent reduction of the edge ion heat flux, caused by the stronger increase of the ion temperature compared to the electron temperature.

This aspect has been analyzed by repeating all of the simulations at 20 MW, 30 MW and 40 MW and with ratio $n_{e,\mathrm{lin}}/n_{e,\mathrm{sep}} \approx 3$ without the inclusion of the $E \times B$ shearing rate in the TGLF–SAT2 input. The comparison of the ion heat fluxes at $\rho_\phi = 1.0$ and $\rho_\phi = 0.9$ are shown in figure 8.

We observe that while at low density the results with and without the inclusion of the $E \times B$ shearing rate are practically equivalent, starting from a certain density value, which decreases with increasing auxiliary electron heating power, the ion heat fluxes at the separatrix computed with the inclusion of the $E \times B$ shearing rate are significantly reduced with respect to those obtained without the inclusion of the $E \times B$ shearing rate. This effect is also visible on the predictions at $\rho_\phi = 0.9$, although less sizeable. The consequence is that there is an uncertainty in the domain of accessibility of the H–mode in the high density domain, where the results with the $E \times B$ shearing rate predict ion heat fluxes which go below the Schmidtmayr scaling at lower densities with respect to those which are obtained without the $E \times B$ shearing rate. The results obtained without the $E \times B$ shearing rate can be considered to more realistically represent conditions of L–mode confinement, whereas the results obtained with the inclusion of the $E \times B$ shearing rate represent conditions in which the transport model in combination with the effect of the shearing practically predicts an L–H transition and the formation of a pedestal. This can be observed in the comparison of the edge profiles with and without the $E \times B$ shearing rate at high density shown in figure 9. The capability of TGLF–SAT2 to predict a pedestal formation for sufficiently large values of the $E \times B$ shearing

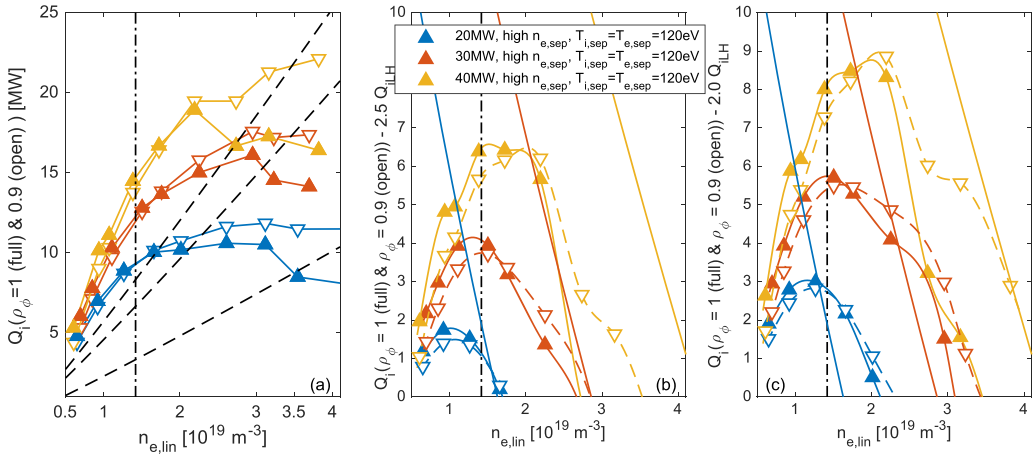

Figure 7. Ion heat flux at $\rho_\phi = 1.0$ (full triangles pointing up) and at $\rho_\phi = 0.9$ (open triangles pointing down) (*a*), the same fluxes minus the L–H transition Schmidtmayr ion heat flux scaling times 2.5 (*b*) and times 2.0 (*c*) as a function of the line averaged density, for hydrogen plasmas with 20 MW, 30 MW and 40 MW ECRH, with $n_{e,\mathrm{sep}} \simeq n_{e,\mathrm{lin}}/3$ and $T_{i,\mathrm{sep}} = T_{e,\mathrm{sep}} = 120$ eV. The vertical dash–dotted line identifies the minimum density according to [17], while the solid oblique lines provide the corresponding ECRH heating power $-2P_{LH,\mathrm{Martin}}$ in MW.

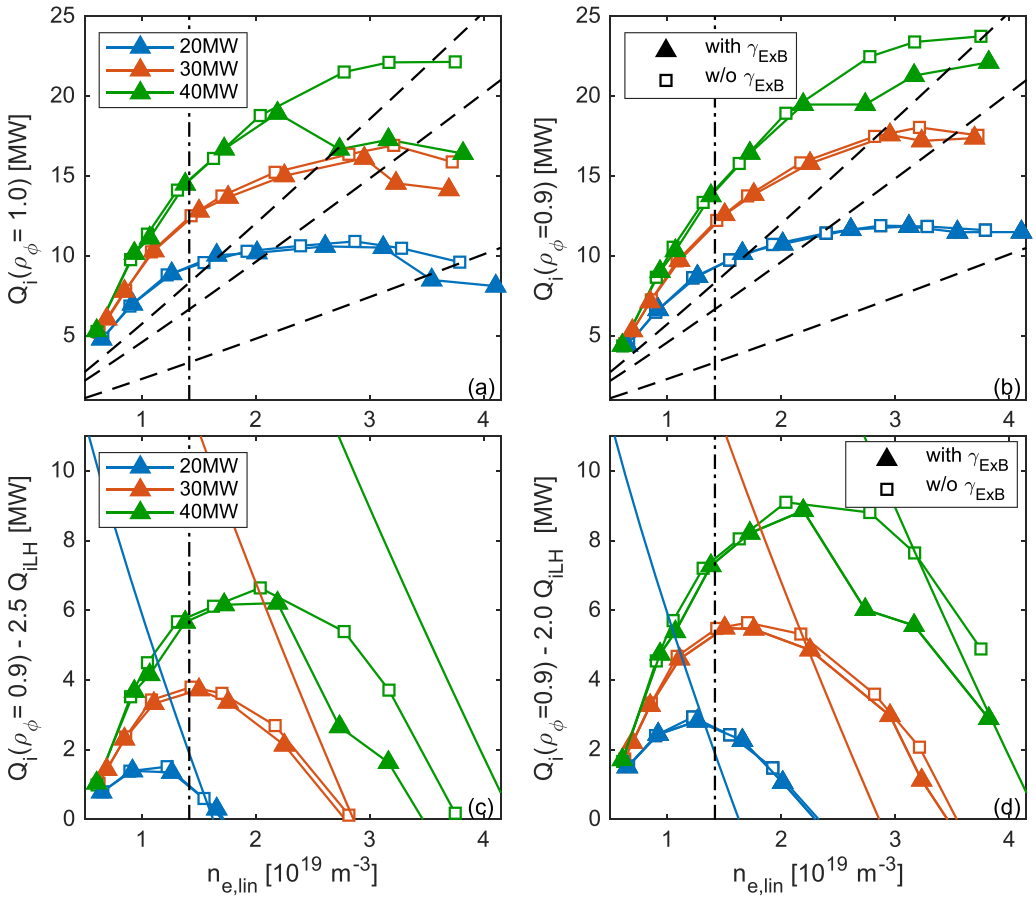

Figure 8. Ion heat fluxes at $\rho_\phi = 1.0$ (*a*) and at $\rho_\phi = 0.9$ (*b*), as well as the same ion heat fluxes at $\rho_\phi = 0.9$ minus the L–H transition Schmidtmayr ion heat flux scaling times 2.5 (*c*) and times 2.0 (*d*), with (full triangles pointing up) and without (open squares) the inclusion of the E × B shearing rate in the TGLF–SAT2 input, as a function of the line averaged density, for hydrogen plasmas with 20 MW, 30 MW and 40 MW ECRH, with $n_{e,\mathrm{sep}} \simeq n_{e,\mathrm{lin}}/3$ and $T_{i,\mathrm{sep}} = T_{e,\mathrm{sep}} = 120$ eV. The vertical dash–dotted line identifies the minimum density according to [17]. In (*a*) and (*b*) the oblique dashed lines provide the deuterium Schmidtmayr scaling for the ion heat flux multiplied by 1, 2 and 2.5. In (*c*) and (*d*) the solid oblique lines provide the corresponding ECRH heating powers $-2P_{LH,\mathrm{Martin}}$ in MW.

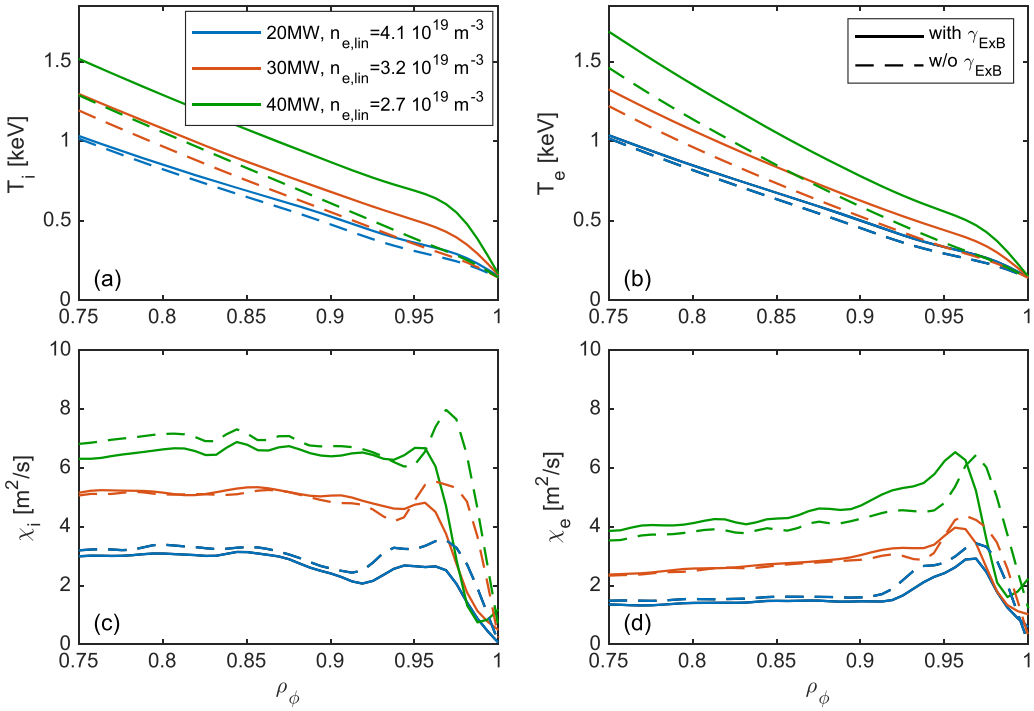

Figure 9. TGLF–SAT2 predicted ion temperature (*a*), electron temperature (*b*), ion heat conductivity (*c*) and electron heat conductivity (*d*) profiles in the outer plasma region as a function of the normalized toroidal minor radius ρ_ϕ with and without the inclusion of the $E \times B$ shearing rate in the TGLF–SAT2 input, at 20 MW, 30 MW and 40 MW of ECRH power and at the corresponding line averaged densities as quoted in the legend.

rate has been recently recognized [52]. This extremely promising element of the TGLF–SAT2 model relies on the validated capability of predicting L–mode profiles up to the separatrix, a necessary condition for the prediction of an edge transport barrier due to turbulence stabilization caused by the equilibrium $E \times B$ shearing rate. Comparisons with nonlinear gyrokinetic results with the GENE code show that the effect of the large $E \times B$ shearing rates produced in these conditions at the plasma edge are underpredicted by TGLF–SAT2, with the consequence that more power than in the experiment is required in TGLF–SAT2 to obtain the pedestal formation. In this respect, while the model cannot be considered realistic regarding the prediction of the heating power requirements, we observe that, qualitatively consistent with present experiments, the model predicts a transition with a pedestal formation with increasing density at fixed electron heating power.

From figures 8 and 9, we also notice that the ion heat flux per particle, which is required to produce the pedestal increases with increasing electron heating power, but also that the pedestal is much stronger at high power than at low power, while the ion temperature increase at low ECRH power is small. The reason for this dependence can be identified in figures 9(*c*) and (*d*), which show that the TGLF–SAT2 predicted heat conductivities increase with increasing ECRH power, and therefore with increasing electron to ion temperature ratio. This feature of TGLF–SAT2 in the modeling of low density electron heated plasmas was already underlined in dedicated modeling of AUG plasmas [30] and was found to be stronger than the results from power balance, which, in contrast, indicated a practically negligible dependence of χ_i on the electron to ion temperature ratio. It can be concluded that the trend predicted by TGLF–SAT2 regarding the requirement of an increased ion heat flux with increasing electron heating power to access the H–mode could be stronger than in reality. We recall that the Schmidtmayr scaling predicts the same ion heat flux per particle for a given magnetic field to produce an L–H transition, regardless the electron heating power. In contrast, the TGLF–SAT2 results would rather suggest that the ion heat flux per particle, which is required to produce the L–H transition, should increase at least linearly with increasing electron heating power. In TGLF–SAT2, since the turbulence is predicted to be more strongly destabilized at high electron heating power, consequently it requires a stronger $E \times B$, and therefore a stronger ion heat flux, to be stabilized. These considerations suggest a dependence which does not appear to be observed in experiments, but which could motivate future experiments to validate or invalidate this expectation.

At the same time, the present analysis on the impact of the $E \times B$ shearing rate shows a modification of the prediction of the high density boundary for H–mode access. The simulations without the inclusion of the $E \times B$ shear provide a more continuous L–mode behavior which appears to be more appropriate for the assessment of the ion heat flux at the edge in the framework of this study. Of course, in reality the $E \times B$ shearing rate increases approaching the L–H transition, and therefore the complete neglect of its effect could give too optimistic projections of the upper boundary of the density window for H–mode access. In the last section, where a summary of the results with comparisons of the different heating conditions are presented and the main conclusions are drawn, we

shall consider the results without the inclusion of the $E \times B$ shearing rate, keeping in mind that this could provide a too optimistic quantification of the upper boundary of the density window. Finally, while such an upper boundary is obtained considering L–mode conditions against the Schmidtmayr scaling, it will be in fact accessed from H–mode conditions in the experiment, therefore with completely different edge transport properties. It can be concluded that the high density boundaries obtained within the present approach certainly have an even larger uncertainty than those at low density.

5. Deuterium plasma at 5 MA and 2.65 T

A final set of simulations has been performed to assess the possibility of entering H–mode in deuterium plasma at 5 MA and 2.65 T, that is, at half of the nominal magnetic field, which will be explored in the initial phase of FPO–1. The simulations have been performed considering the planned geometry of the ITER horizontal and vertical ECRH launchers, with 20 MW deposited on–axis, at $\rho_\phi = 0.1$, and 20 MW deposited off–axis, at $\rho_\phi = 0.5$. In this case, we focus on the results without the inclusion of $E \times B$ shearing, which ensures L–mode like conditions over the entire density range which has been explored at this relatively high heating power.

Analogously to what has been observed for the hydrogen density scans in figure 8 at the end of the previous session, also in these density scans in deuterium plasmas the inclusion of the $E \times B$ shearing produces the development of an edge pedestal for line average densities above 2 10^{19} m^{-3}. Correspondingly, the predicted ion heat fluxes are reduced, caused by the drop of the difference between the electron and the ion temperatures at the edge, similar to the results shown in figure 9. As already mentioned, results in figure 10 are only shown without the inclusion of the $E \times B$ shearing rate, ensuring L–mode conditions in the simulations.

The analysis of figure 11 shows that with 40 MW of ECRH power in deuterium at 2.65 T the predicted H-mode access window is only limited by the Greenwald density limit at high density, and not by the crossing between the available ion heat flux and the Schmidtmayr scaling. This situation is clearly more favorable than all the conditions that have been examined in hydrogen. The significantly lower slope of the threshold ion heat flux with increasing density in deuterium, even in the presence of a higher magnetic field, allows the TGLF–SAT2 predicted ion heat flux to be only crossed at a line averaged density around 6 10^{19} m^{-3}, well above the Greenwald density limit and not too far below the density at which the power of 40 MW crosses the Martin scaling for the L–H power threshold, which is located at 7.3 10^{19} m^{-3}. Despite the higher magnetic field of the deuterium scenario, the excess in ion heat flux with respect to the Schmidtmayr scaling is predicted to be above 6.5 MW in a relatively large density window, which practically extends from the value of the Ryter scaling for the density minimum, 1.80 10^{19} m^{-3}, marked with a vertical dash–dotted line in figure 11(*b*), up to the density limit. Finally we notice that, similarly to the hydrogen cases shown in sections 2 and 3, the assumption of an increased ion temperature at the separatrix implies a significant reduction of the predicted ion heat flux at the edge. However, even in the particularly unfavorable condition of $T_{i,\mathrm{sep}} = 200$ eV, a relatively large density window for H–mode access remains available, with an excess in ion heat flux up to 5 MW, pretty well centered around the Ryter minimum density.

6. Impact of the presence of tungsten

So far it has been assumed that the impurity composition is only provided by beryllium. The impact of an additional radiating impurity, neon, has been tested in hydrogen plasmas with 20 MW of ECRH in section 3.2. In view of the recently introduced possibility of having a full tungsten wall in ITER, in this section the impact of an increase in tungsten concentration is considered. In order to keep the simulations sufficiently fast, the number of ion species in the TGLF–SAT2 input is still kept equal to 2. Therefore we have repeated a subset of the simulations replacing the 0.042 concentration of beryllium, providing an effective charge of 1.5, with tungsten at two different levels of concentrations, $c_W = n_W/n_e = 10^{-5}$ and $c_W = 10^{-4}$, representing low and relatively high concentrations respectively. The corresponding radiated power has been included in the electron heat sources. For comparison, both a 30 MW ECRH plasma in hydrogen and a 40 MW ECRH plasma in deuterium have been considered. The results for the hydrogen and deuterium plasmas are presented in figures 12 and 13 respectively. Consistent with the results presented in section 3.2, the replacement of a relatively larger amount of light impurity (beryllium producing a $\Delta Z_{\mathrm{eff}} = 0.5$) with a 10^{-5} concentration of tungsten (corresponding to $\Delta Z_{\mathrm{eff}} < 0.02$) in a hydrogen plasma implies an increase of the electron to ion thermal coupling, as a consequence of the higher charge to mass ratio of hydrogen in comparison to that of beryllium. The ion heat flux is also increased by the increase of the TGLF–SAT2 ion heat conductivity, produced by the reduced impurity dilution and the consequent ion temperature drop in plasmas with a tungsten impurity in comparison with plasmas with a beryllium impurity. Therefore the removal of beryllium and the inclusion of a very small amount of W can be considered to lead to an increase, or at least not to a reduction, of the density window and of the ion heat flux excess to access H–mode. In contrast, in case of a 10^{-4} tungsten concentration, a significant increase of the radiated power, shown with dash–dotted lines and full diamonds in figure 12(*a*), effectively implies a non–negligible reduction of the net electron heating power, leading also to a reduction of the electron temperature and of the total electron to ion heat flux with increasing density. This leads to the prediction of a significant reduction of the upper boundary of the density window, particularly in case the H–mode access is already allowed at 2 times the deuterium Schmidtmayr scaling (dashed lines with squares in figure 12(*b*)). As already mentioned, these simulations have been performed with constant tungsten concentration to provide an estimate of the impact of this impurity on the predictions. The values of a relatively low concentration of 10^{-5} and of an already considerable concentration of 10^{-4}

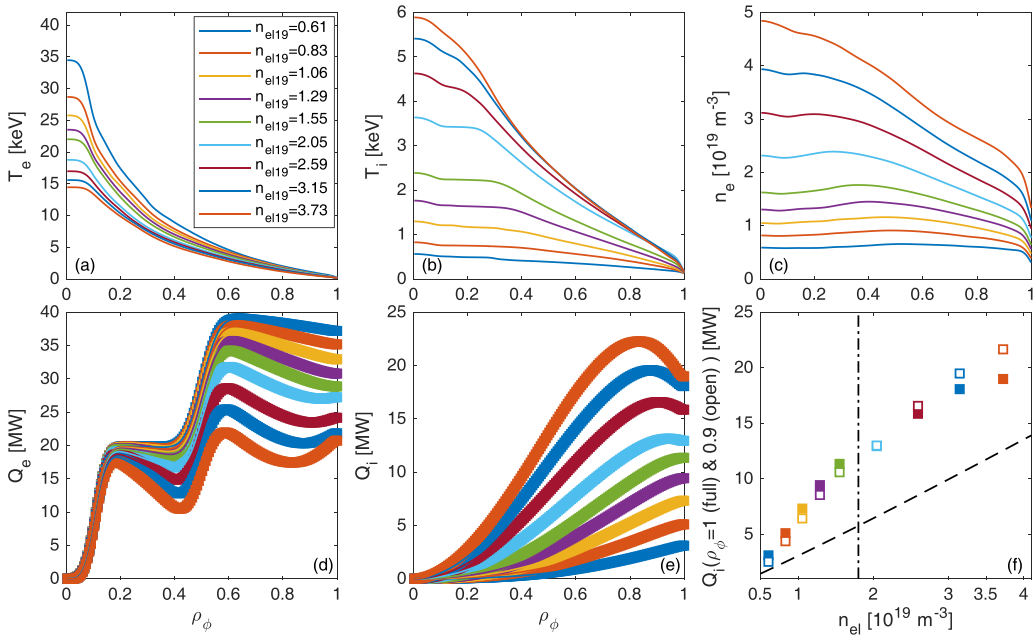

Figure 10. ASTRA/TGLF–SAT2 predictions of the electron temperature (*a*), the ion temperature (*b*) in keV, and the electron density (*c*) in 10^{19} m^{-3} in ITER deuterium plasmas at 5 MA and 2.65 T, with 40 MW of ECRH power as a function of the normalized toroidal minor radius ρ_ϕ, for different values of the line averaged electron density, reported in the legend. The corresponding profiles of the electron and ion heat fluxes are presented in (*d*) and (*e*). In (*f*) the corresponding values of the ion heat fluxes at $\rho_\phi = 1$ and $\rho_\phi = 0.9$ are plotted as a function of the line averaged density. In (*f*) the oblique dashed line correspond to the Schmidtmayr scaling for the ion heat flux for the L–H transition, while the vertical dash–dotted line identifies the line averaged density value where the minimum density is expected to occur according to [17].

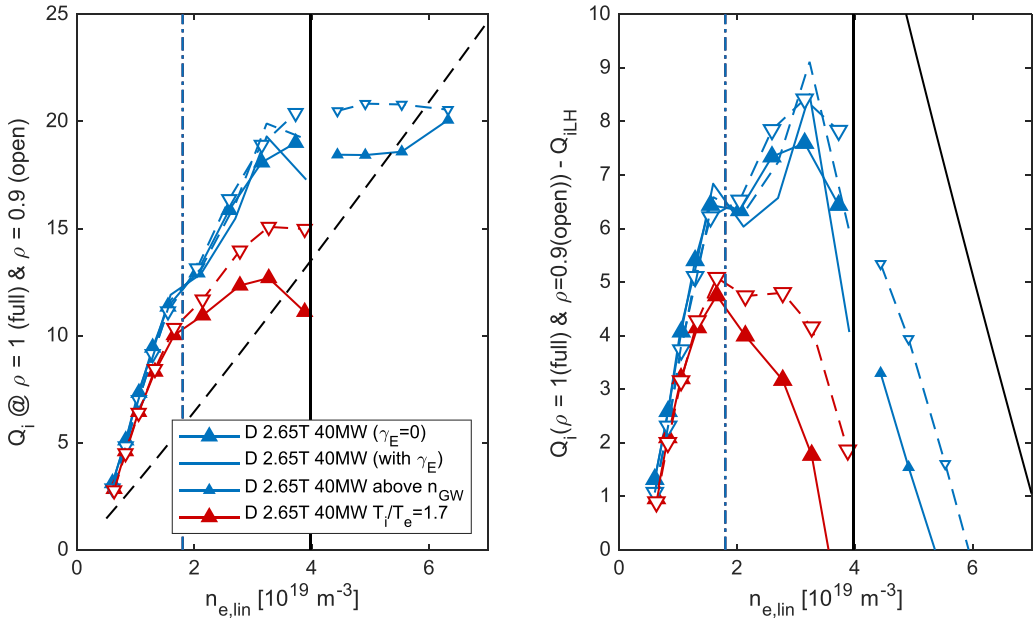

Figure 11. Ion heat fluxes in MW at $\rho_\phi = 1.0$ (full triangles pointing up) and at $\rho_\phi = 0.9$ (open triangles pointing down) (*a*), the same fluxes minus the L–H transition Schmidtmayr ion heat flux scaling (*b*) as a function of the line averaged density, for deuterium plasmas with 40 MW ECRH and with $n_{e,\mathrm{sep}} \simeq n_{e,\mathrm{lin}}/2.5$ and $T_{i,\mathrm{sep}} = T_{e,\mathrm{sep}} = 120$ eV, with (solid and dashed lines at $\rho_\phi = 1.0$ and $\rho_\phi = 0.9$ respecticaly without markers) and without (solid and dashed lines with full and open markers) the inclusion of the $E \times B$ shearing rate. Additionally, results with $T_{i,\mathrm{sep}} = 200$ eV and $T_{e,\mathrm{sep}} = 120$ eV are presented with symbols as described in the legend. The vertical dash–dotted line identifies the minimum density according to [17], while the solid oblique line in (*b*) provides $40 - P_{LH,\mathrm{Martin}}$, finally the vertical solid line identifies the Greenwald density limit. The line averaged density values above the Greenwald density limit (plotted with small symbols) have been computed to compare the density at which the predicted ion heat flux by TGLF–SAT2 exceeds the Schmidtmayr scaling for the ion heat flux with the density at which 40 MW exceed the Martin scaling for P_{LH}.

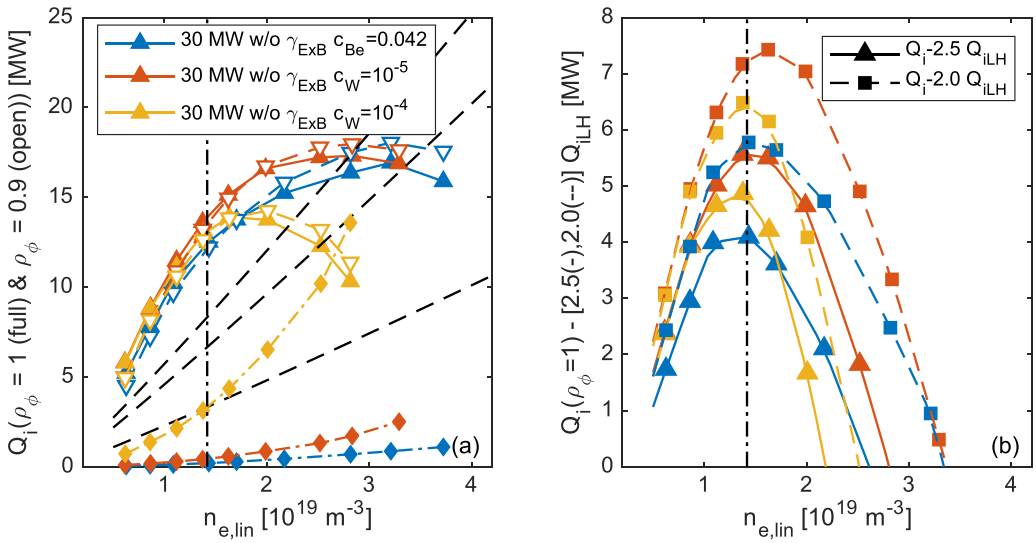

Figure 12. Ion heat fluxes in MW at $\rho_\phi = 1.0$ (full squares) and at $\rho_\phi = 0.9$ (open circles) (*a*), the same fluxes minus the L–H transition Schmidtmayr ion heat flux scaling, times 2.0 and 2.5 for these hydrogen cases, (*b*) as a function of the line averaged density, for hydrogen plasmas at 1.7 T with 30 MW ECRH, $n_{e,\mathrm{sep}} \simeq n_{e,\mathrm{lin}}/3$ and $T_{i,\mathrm{sep}} = T_{e,\mathrm{sep}} = 120$ eV, without the inclusion of the impact of the $E \times B$ shearing rate in TGLF–SAT2, for different additional impurity species, with beryllium concentration of 0.042, same result as in figure 8, and with tungsten in concentration 10^{-5} and 10^{-4}. In (*a*) the full diamonds with dash–dotted lines show the corresponding total radiated powers in MW, with the same color code as in the legend. In (*a*) the dashed oblique lines show 1, 2, and 2.5 times the Schmidtmayr scaling, whereas the vertical dash–dotted lines identify the minimum density according to [17].

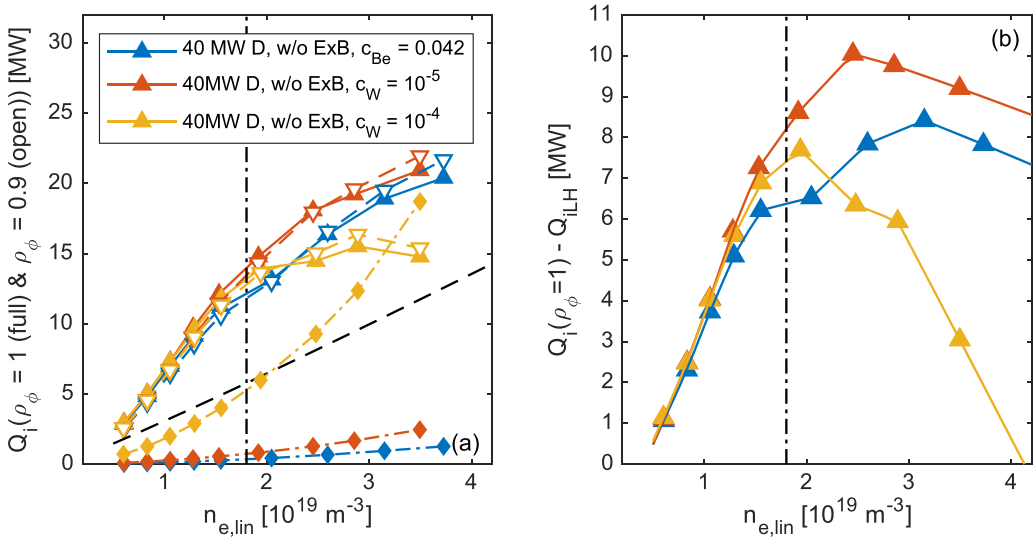

Figure 13. Ion heat fluxes in MW at $\rho_\phi = 1.0$ (full squares) and at $\rho_\phi = 0.9$ (open circles) (*a*), the same fluxes minus the L–H transition Schmidtmayr ion heat flux scaling, times 2.0 and 2.5 for these hydrogen cases, (*b*) as a function of the line averaged density, for hydrogen plasmas at 1.7 T with 30 MW ECRH, $n_{e,\mathrm{sep}} \simeq n_{e,\mathrm{lin}}/2.5$ and $T_{i,\mathrm{sep}} = T_{e,\mathrm{sep}} = 120$ eV, without the inclusion of the impact of the $E \times B$ shearing rate in TGLF–SAT2, for different additional impurity species, with beryllium concentration of 0.042, same result as in figure , and with tungsten in concentration 10^{-5} and 10^{-4}. In (*a*) the dashed oblique line shows the Schmidtmayr scaling, whereas the vertical dash–dotted lines identify the minimum density according to [17].

have been considered (concentrations above 10^{-3} are usually unlikely to be sustainable by the plasma). The task of predicting the actual tungsten concentration in the ITER PFPO phase is certainly not easy, but it can be reasonably expected that the tungsten concentration will decrease with increasing plasma density. This would lead to the prediction that while at low density relatively large concentrations, in the range of 10^{-4}, will not strongly impact the H–mode access, at high density lower concentrations, in the range of few 10^{-5}, would not have a particularly unfavorable effect.

Moving now to the analysis of the impact of a tungsten concentration of 10^{-5} and 10^{-4} in a 40 MW ECRH deuterium plasma at 5 MA and 2.65 T, shown in figure 13, we observe that the effect of the increased radiated power at high density leads to results which are analogous to those obtained in hydrogen. However, differently from the situation in hydrogen,

and consistent with the analysis presented in section 3.2, the replacement of beryllium with tungsten, even at low concentration, does not significantly affect the prediction of the H–mode access at low density. Because deuterium and berillyium have the same charge to mass ratio, the removal of beryllium does not lead to an increase of the electron to ion thermal coupling. At the same time, the impact of a reduction of the impurity dilution in the heat transport predicted by TGLF–SAT2 remains visible, leading to a decrease of the ion temperature and a consequent increase of the ion heat flux. This effect is non-negligible at intermediate densities. Finally, consistently with the results in hydrogen, a fixed tungsten concentration of 10^{-4} significantly increases the radiated power at high density and reduces the upper boundary of the density window. This now becomes close to the Greenwald density limit, with also a significant reduction of the excess of ion heat flux with increasing density. Again, it is reasonable to expect that the tungsten concentration will decrease with increasing density, mitigating this effect.

Overall, it can be concluded that the replacement of beryllium with tungsten can be expected to produce an increase of the ion heat flux excess above threshold at low density, more significant in hydrogen than in deuterium, and should not be expected to produce a considerable reduction of the upper boundary of the density window for H–mode access in both 5 MA/1.7 T operation in hydrogen and 5 MA/2.65 T operation in deuterium, provided the tungsten concentration can be kept well below 10^{-4} in these conditions.

7. Conclusions

In order to predict the power threshold for the L–H transition in ITER low density plasmas with ECRH only, the strategy which has been followed in this work follows AUG [17] and C–Mod results [20] which identify the ion heat flux as the relevant quantity which determines the L–H transition. Thereby, the low density branch in electron heated plasmas is the consequence of the reduced coupling between electrons and ions at low density and high electron temperature [17, 18]. Within this paradigm, the access to H–mode in low density electron heated plasmas is connected with the possibility of producing sufficient ion heat flux at the edge by electron–ion thermal coupling. Transport simulations can then be performed to predict temperature and density profiles and the consequent equipartition power and the predicted ion heat flux can be compared with the AUG and C–Mod scaling proposed in [20]. Considering that this scaling for the critical ion heat flux to access H–mode has been obtained for deuterium plasmas, an additional factor larger than one has to be introduced in hydrogen plasmas to take into account the impact on the ion heat flux threshold of the change from deuterium to hydrogen, as experimentally observed.

It is important to underline that, still within the main paradigm provided by the assumption that the L–H transition is caused by turbulence stabilization from a sufficiently large $E \times B$ shearing, produced by an equilibrium radial electric field, the applied strategy is exclusively based on the criterion of the minimum ion heat flux for the transition, and does not take into account additional effects which could impact the L–H transition requirements in ITER as compared to present devices. In particular, potentially different edge intrinsic toroidal rotations as well as edge poloidal rotations, which would not be mainly proportional to the main ion temperature gradient and therefore which cannot be at least partly captured by a criterion based on a ion heat flux threshold, are not included in the present approach. Moreover, effects produced by thermal ion orbit losses, which could have different impact on the radial electric field in ITER in comparison to AUG and C–Mod conditions, are also neglected in the present approach. It is also worthwhile to mention that this work does not address either whether the impact of resonant Magnetic Perturbations (MP) for Edge Localized Mode (ELM) suppression could significantly alter the predicted density windows over which, at the various considered ECRH powers, an L–H transition can be expected to take place. Several works in present devices [53–58] have demonstrated that the application of MPs can increase the power threshold up to a factor of two, depending on the amplitude of the applied magnetic field perturbation as well as on the density range. Within the framework of a required $E \times B$ shear to enter H–mode, it can be considered that if the MPs produce a flattening of the main ion pressure profile, a higher heating power is required to achieve the required conditions to produce the L–H transition. Recent results in AUG [58] have shown that the minimum value of the relative amplitude of the magnetic field perturbation, which is required to obtain ELM suppression, is lower than the value above which an approximately linear increase of the L–H power threshold with increasing relative MP amplitude is observed. At present it is still unclear how these two values of the relative MP amplitude separately extrapolate, when moving from the conditions of present tokamaks to ITER. However, if a finite window between these two critical values exists also in ITER, this could allow ELM suppression by applying the MP already during the L–mode phase and without affecting the required conditions to enter H–mode.

Following the assumed strategy, which is based on a critical ion heat flux for the L–H transition, in this paper a set of ASTRA/TGLF–SAT2 full–radius simulations has been performed to predict the ion heat flux at the edge in the initial PFPO–1 and FPO–1 phases of the ITER research plan, with auxiliary heating only provided by ECRH. In these heating conditions, the ion heat flux at the edge is exclusively provided by the electron to ion heat exchange and therefore completely determined by the transport properties of the plasma. The predicted ion heat fluxes have been compared with the expectations for H–mode access obtained from the recent scaling for the H–mode ion heat flux threshold based on a combined database of AUG and C–Mod observations. Several ITER scenarios have been explored, always with 5 MA current, and with 1.8 T in hydrogen and 2.65 T in deuterium.

A comparison of the main scenarios that have been considered is presented in figure 14. In this selection we have excluded the 20 MW ECRH power hydrogen cases, which provide an almost vanishing H–mode operational window, and focused on the more promising conditions with 30 MW

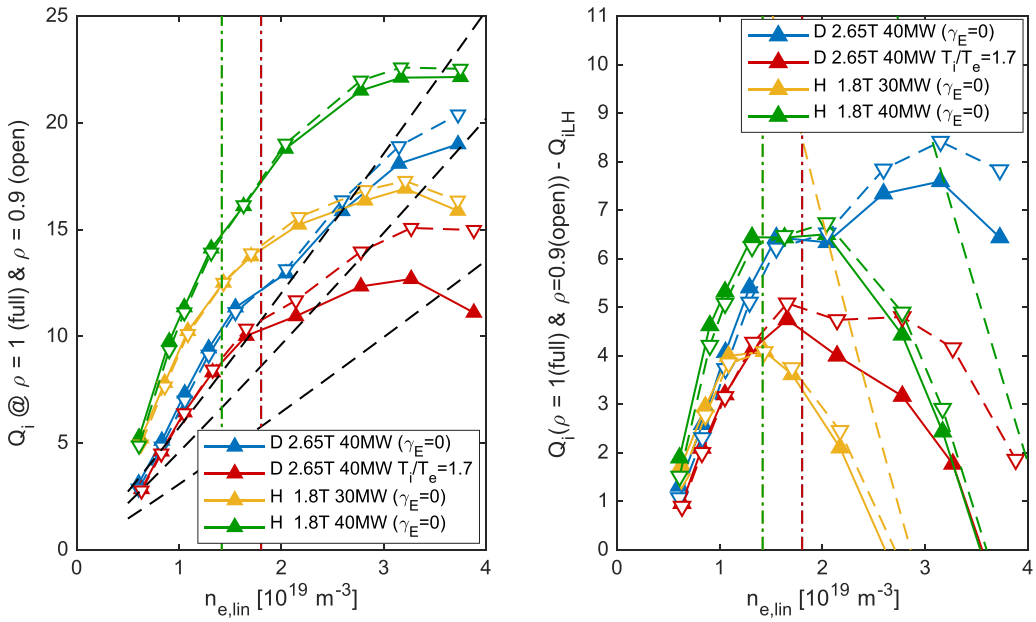

Figure 14. Ion heat fluxes in MW at $\rho_\phi = 1.0$ (full triangles pointing up) and at $\rho_\phi = 0.9$ (open triangles pointing down) (*a*), the same fluxes minus the L–H transition Schmidtmayr ion heat flux scaling (times 2.5 for the hydrogen cases) (*b*) as a function of the line averaged density, for deuterium plasmas at 2.65 T with 40 MW ECRH, $n_{e,\mathrm{sep}} \simeq n_{e,\mathrm{lin}}/2.5$ and $T_{i,\mathrm{sep}} = T_{e,\mathrm{sep}} = 120$ eV, as well as with 40 MW ECRH, $T_{i,\mathrm{sep}} = 200$ eV and $T_{e,\mathrm{sep}} = 120$ eV, and hydrogen plasmas at 1.8 T with $T_{i,\mathrm{sep}} = T_{e,\mathrm{sep}} = 120$ eV and 30 MW and 40 MW ECRH, and with $n_{e,\mathrm{sep}} \simeq n_{e,\mathrm{lin}}/3$, with symbols as reported in the legend. The vertical dash–dotted lines identify the minimum densities according to [17] at 1.8 T and 2.65 T. The dashed oblique lines in (*a*) show 1, 2, and 2.5 times the Schmidtmayr scaling for the deuterium ion heat flux, while the dashed oblique lines in (*b*) provide $20 - 2P_{LH,\mathrm{Martin}}$ MW, and $30 - 2P_{LH,\mathrm{Martin}}$ MW for the hydrogen cases, while the line $40 - P_{LH,\mathrm{Martin}}$ falls out of the maximum *x*–axis, which corresponds to the Greenwald density limit.

ECRH power in hydrogen at 1.8 T and 40 MW ECRH power in deuterium at 2.65 T, always at 5 MA. For additional comparison, we have also included the 40 MW ECRH power cases in hydrogen at 1.8 T and the 40 MW deuterium case with $T_{i,\mathrm{sep}} = 1.7 T_{e.\mathrm{sep}}$. All the other scenarios have been considered with $T_{i,\mathrm{sep}} = T_{e.\mathrm{sep}} = 120$ eV, and, in figure 14, only the results with ratios between the line averaged density and the separatrix density around 3 and the removal of the $E \times B$ shearing rate in the TGLF–SAT2 input are shown.

The first important conclusion is that for hydrogen plasmas at 1.8 T, while 20 MW ECRH cannot be expected to allow stable H–mode operation, a small but likely sufficient operational window for operation in H–mode in hydrogen is predicted at 30 MW of ECRH power and a wider one with 40 MW. The most favorable condition is obtained around the minimum density predicted by the Ryter scaling, that is at a line averaged density around 1.4 10^{19} m^{-3}, and in any case below 2.5 10^{19} m^{-3}, corresponding to 0.6 the Greenwald density limit at 5 MA. A vanishing H–mode operational window at 20 MW ECRH is consistent with the direct application of the Martin's scaling, increased by a factor 2 to account for hydrogen operation, at the density minimum of the Ryter scaling, corresponding to 0.35 of the Greenwald limit at 5 MA. This provides a power threshold of 17.4 MW. The same conclusion was reached in [32, 33], where the Martin's scaling with a factor 2 for hydrogen was applied at 0.4 the Greenwald limit, which yields a threshold of 18.8 MW.

The second conclusion is that, in deuterium plasmas at 2.65 T and 5 MA, 40 MW of ECRH power, with 20 MW on axis and 20 MW at mid–radius, are predicted to allow a substantial H–mode operational window, the widest one of all 5 MA plasmas modeled, with upper boundary in the density window robustly provided by the density limit and not by the L–H power threshold.

The last, certainly important and general, conclusion is that, as a consequence of the shape of the dependence of the edge ion heat flux as a function of the line averaged density, which saturates at high density, in comparison to the dependence of the critical ion heat flux, which is practically linear in density, deuterium plasmas allow a significantly broader density window to access H–mode than hydrogen plasma. This is caused by the significantly stronger slope of the ion heat flux threshold in hydrogen, in spite of the fact that deuterium plasmas have a thermal exchange between electrons and ions which is half of that of hydrogen and have been considered with a higher magnetic field. As it is clearly shown in figure 14, even in the case of the hydrogen plasmas with 40 MW ECRH power at 1.8 T and an assumption of the hydrogen ion heat flux threshold equal to two times the Schmidtmayr scaling, the H–mode operational window would be significantly more limited in power at high density as compared to the deuterium 40 MW ECRH power case at 2.65 T. With a threshold at 2.5 times the Schmidtmayr scaling for hydrogen, which is more consistent with present available results in hydrogen plasmas, even with 40 MW ECRH, the H–mode operational window in hydrogen is predicted to have an upper boundary in density which is below the Greenwald density limit.

These general conclusions have important implications in the event that, instead of the Greenwald scaling, the density limit follows the recently proposed, theoretically based, scaling for the edge density, which also depends on the power through the separatrix [59]. For ITER this scaling predicts an edge density limit of 8.5 10^{19} m^{-3} at 5 MA, 1.7 T and 30 MW, and of 9.5 10^{19} m^{-3} at 5 MA, 2.65 T and 40 MW. It can be concluded that this recent formula for the edge density limit forsees that densities at least a factor 2 higher than those predicted by the Greenwald limit for the line averaged density will be accessible in these low current ITER plasmas. This significant difference, however, would not affect the density windows to access H–mode which have been obtained in this work in hydrogen plasmas, since, even at 40 MW, these are in any case limited at high density by the increase of the L–H power threshold with increasing density, before the value of the density limit be reached. In contrast, the increased density limit predicted by [59] could provide a broader window of H–mode operation in deuterium at 40 MW of ECRH power. In this case, the H–mode operational window in deuterium at 5 MA, 2.65 T and 40 MW would also become limited by the L–H power threshold increase with increasing density, which is at the line averaged density of 7.2 10^{19} m^{-3} according to the Martin's scaling, and not by the density limit itself, since, according to [59], this would be in any case at even higher densities. In this context, we recall that the upper boundary of the density window for H–mode access, which is determined in this work, should be considered to be affected by higher uncertainties than the lower density boundary. These higher uncertainties are in particular produced by the larger radial variation of the ion heat flux at the edge at high density and the possible increase of the ion temperature with increasing density, caused by the concomitant increase of the $E \times B$ shearing rate. An increase of the ion temperature would reduce the ion heat flux from the electron to ion thermal coupling and the upper density boundary, where the predicted ion heat flux crosses the Schmidtmayr scaling.

The replacement of a beryllium impurity with a tungsten impurity in concentrations between 10^{-5} and 10^{-4} has been found to increase the ion heat flux excess above the Schmidtmayr threshold at low density. This effect is more significant in hydrogen than in deuterium. The increased radiation leads to a reduction of the upper boundary of the density window for H–mode access in both 5 MA/1.7 T operation in hydrogen and 5 MA/2.65 T operation in deuterium. This reduction, however, remains limited, provided the tungsten concentration can be kept well below 10^{-4} in these conditions.

As a final remark, we underline that this work has been exclusively dedicated to the modeling of the transport properties of the confined plasmas, prescribing values of the separatrix density as boundary condition. The assessment of the compatibility of the assumed separatrix densities with the requirements for power exhaust has been considered to be out of the scope of this work.

Acknowledgment

C.A is grateful to U. Plank and F. Ryter for several very fruitful discussions on the experimental properties of the L–H transition and on the power threshold dependencies, as well as to N. Bonanomi for very useful interactions on the properties of the formation of an edge pedestal in the ASTRA simulations with the TGLF–SAT2 model. The Authors are also grateful to G.M. Staebler for the development of the TGLF–SAT2 model and for his advice on the application of this model, as well as to the colleagues of the ITPA Topical Group Transport and Confinement, Joint Activity 31, and of the EUROfusion task TSVV11 for fruitful and motivating discussions. This work has been carried out within the framework of the EUROfusion Consortium, funded by the European Union via the Euratom Research and Training Programme (Grant Agreement No 10105220—EUROfusion). Views and opinions expressed are however those of the authors only and do not necessarily reflect those of the European Union of the European Commission. Neither the European Union nor the European Commission can be held responsible for them. Moreover, the views and opinions expressed herein do not necessarily reflect those of the ITER Organization.

ORCID iDs

C. Angioni https://orcid.org/0000-0003-0270-9630
J. Citrin https://orcid.org/0000-0001-8007-5501
A. Loarte https://orcid.org/0000-0001-9592-1117
E. Fable https://orcid.org/0000-0001-5019-9685

References

[1] ITER Research Plan 2018 *ITER Technical Report* ITR-18-03 (ITER Organization) (available at: www.iter.org/doc/www/content/com/Lists/ITER%20Technical%20Reports/Attachments/9/ITER-Research-Plan_final_ITR_FINAL-Cover_High-Res.pdf)
[2] Loarte A. *et al* 2021 *Nucl. Fusion* **61** 076012
[3] Snipes J.A. *et al* 1996 *Nucl. Fusion* **36** 1217
[4] Andrew Y. *et al* 2006 *Plasma Phys. Control. Fusion* **48** 479
[5] Ryter F. *et al* 2009 *Nucl. Fusion* **49** 062003
[6] Ma Y., Hughes J.W., Hubbard A.E., LaBombard B., Churchill R.M., Golfinopolous T., Tsujii N. and Marmar E.S. 2012 *Nucl. Fusion* **52** 023010
[7] Ryter F. *et al* 2013 *Nucl. Fusion* **53** 113003
[8] Maggi C.F. *et al* 2014 *Nucl. Fusion* **54** 023007
[9] Vincenzi P. *et al* 2022 *Plasma Phys. Control. Fusion* **64** 124004
[10] Martin Y.R. and Takizuka T. (The ITPA CDBM H-mode Threshold Data Working Group) 2008 *J. Phys.: Conf. Ser.* **123** 012033
[11] Biglari H., Diamond P.H. and Terry P.W. 1990 *Phys. Fluids* B **2** 1
[12] Groebner R.J., Burrell K.H. and Seraydarian R.P. 1990 *Phys. Rev. Lett.* **64** 3015
[13] Burrell K.H. *et al* 1997 *Phys. Plasmas* **4** 1499
[14] Hinton F.L. 1985 *Nucl. Fusion* **25** 1457
[15] deGrassie J.S., deGrassie J.S., Boedo J.A. and Grierson B.A. 2015 *Phys. Plasmas* **22** 080701

[16] Diamond P.H., Itoh S.-I., Itoh K. and Hahm T.S. 2005 *Plasma Phys. Control. Fusion* **47** R35
[17] Ryter F., Barrera Orte L., Kurzan B., McDermott R.M., Tardini G., Viezzer E., Bernert M. and Fischer R. 2014 *Nucl. Fusion* **54** 083003
[18] Bilato R., Angioni C., Birkenmeier G. and Ryter F. (ASDEX Upgrade Team) 2020 *Nucl. Fusion* **60** 124003
[19] Ryter F. *et al* 2016 *Plasma Phys. Control. Fusion* **58** 014007
[20] Schmidtmayr M. *et al* 2018 *Nucl. Fusion* **58** 056003
[21] ITER Physics Expert Group on Confinement and Transport and Confinement Modelling and Database, ITER Physics Basis Editors 1999 *Nucl. Fusion* **39** 2175
[22] Pereverzev G.V., Yushmanov P.N. 2002 *ASTRA, Automated System for Transport Analysis in a Tokamak (IPP 5/98)* Max–Planck–Instituet für Plasmaphysik
[23] Fable E. *et al* 2013 *Plasma Phys. Control. Fusion* **55** 124028
[24] Staebler G.M., Candy J., Belli E.A., Kinsey J.E., Bonanomi N. and Patel B. 2021 *Plasma Phys. Control. Fusion* **63** 015013
[25] Staebler G.M. *et al* 2021 *Nucl. Fusion* **61** 116007
[26] Staebler G.M., Kinsey J.E. and Waltz R.E. 2005 *Phys. Plasmas* **12** 102508
[27] Staebler G.M. *et al* 2007 *Phys. Plasmas* **14** 055909
[28] Angioni C. *et al* 2022 *Nucl. Fusion* **62** 066015
[29] Angioni C., Bonanomi N., Fable E., Schneider P.A., Tardini G., Luda T. and Staebler G.M. 2023 *Nucl. Fusion* **63** 056005
[30] Kiefer C.K., Angioni C., Tardini G., Bonanomi N., Geiger B., Mantica P., Pütterich T., Fable E. and Schneider P.A. 2021 *Nucl. Fusion* **61** 066035
[31] Romanelli M. *et al* 2014 *Plasma Fusion Res.* **9** 3403023
[32] Militello Asp E. *et al* 2020 *IAEA Fus. Energy Conf. 2020* (*Virtual Conference, 10–15 May 2021)* p 1104 (available at: https://nucleus.iaea.org/sites/fusionportal/Shared Documents/FEC 2020/fec2020-preprints/preprint1104.pdf)
[33] Tholerus E. *et al* 2021 *EPS DPP Conf.* (*Virtual Conference, 21–25 June 2021)* p 4.1057 (available at: http://ocs.ciemat.es/EPS2021PAP/pdf/P4.1057.pdf)
[34] Polevoi A.R. *et al* 2023 *Nucl. Fusion* **63** 076003
[35] Bourdelle C. *et al* 2014 *Nucl. Fusion* **54** 022001
[36] Shao L.M. *et al* 2016 *Plasma Phys. Control. Fusion* **58** 025004
[37] Plank U. *et al* 2020 *Nucl. Fusion* **60** 074001
[38] Plank U. *et al* 2023 *Plasma Phys. Control. Fusion* **65** 014001
[39] Righi E. *et al* 1999 *Nucl. Fusion* **39** 309
[40] Gohil P. , Evans T.E., Fenstermacher M.E., Ferron J.R., Osborne T.H., Park J.M., Schmitz O., Scoville J.T. and Unterberg E.A. 2011 *Nucl. Fusion* **51** 103020
[41] Maggi C.F. *et al* 2018 *Plasma Phys. Control. Fusion* **60** 014045
[42] Birkenmeier G. *et al* 2022 *Nucl. Fusion* **62** 086005
[43] Schmitz L. *et al* 2022 *Nucl. Fusion* **62** 126050
[44] Pacher H.D., Kukushkin A.S., Pacher G.W., Kotov V., Pitts R.A. and Reiter D. 2015 *J. Nucl. Mater.* **463** 591–5
[45] Greenwald M. 2002 *Plasma Phys. Control. Fusion* **44** R27–R53
[46] Houlberg W.A., Shaing K.C., Hirshman S.P. and Zarnstorff M.C. 1997 *Phys. Plasmas* **4** 3230
[47] Pereverzev G.V. and Corrigan G. 2008 *Comp. Phys. Commun.* **179** 579–85
[48] Angioni C., Fable E., Greenwald M., Maslov M., Peeters A.G., Takenaga H. and Weisen H. 2009 *Plasma Phys. Control. Fusion* **51** 124017
[49] Fable E., Angioni C. and Sauter O. 2010 *Plasma Phys. Control. Fusion* **52** 015007
[50] Angioni C., Peeters A.G., Garbet X., Manini A. and Ryter F. (ASDEX Upgrade Team) 2004 *Nucl. Fusion* **44** 827
[51] Angioni C., Fable E., Manas P., Mantica P. and Schneider P.A. 2018 *Phys. Plasmas* **25** 082517
[52] Bonanomi N. *et al* 2022 *EPS Conf.* O5.101 (available at: https://indico.fusenet.eu/event/28/contributions/281/)
[53] Ryter F., Rathgeber S.K., Viezzer E., Suttrop W., Burckhart A., Fischer R., Kurzan B., Potzel S. and Pütterich T. 2012 *Nucl. Fusion* **52** 0114014
[54] Mordijck S., Nakatsutsumi M., Pelka A., Priebe G., Thorpe I. and Tschentscher T. 2015 *Plasma Phys. Control. Fusion* **57** 014003
[55] Scannel R., Kirk A., Carr M., Hawke J., Henderson S.S., O'Gorman T., Patel A., Shaw A. and Thornton A. 2015 *Plasma Phys. Control. Fusion* **57** 075013
[56] Park H. *et al* 2019 *Nucl. Fusion* **59** 112020
[57] Schmitz L. *et al* 2019 *Nucl. Fusion* **59** 126010
[58] Willensdorfer M. *et al* 2022 *Phys. Plasmas* **29** 032506
[59] Giacomin M., Pau A., Ricci P., Sauter O. and Eich T., (The ASDEX Upgrade team, JET Contributors and The TCV team) 2022 *Phys. Rev. Lett.* **128** 185003